ARMY RESEARCH LABORATORY

High-Maneuverability Airframe: Initial Investigation of Configuration's Aft End for Increased Stability, Range, and Maneuverability

by Sidra I. Silton and Frank Fresconi

ARL-TR-6585 **September 2013**

Approved for public release; distribution is unlimited.

NOTICES

Disclaimers

The findings in this report are not to be construed as an official Department of the Army position unless so designated by other authorized documents.

Citation of manufacturer's or trade names does not constitute an official endorsement or approval of the use thereof.

Destroy this report when it is no longer needed. Do not return it to the originator.

Army Research Laboratory
Aberdeen Proving Ground, MD 21005-5066

ARL-TR-6585 **September 2013**

High-Maneuverability Airframe: Initial Investigation of Configuration's Aft End for Increased Stability, Range, and Maneuverability

Sidra I. Silton and Frank Fresconi
Weapons and Materials Research Directorate, ARL

Approved for public release; distribution is unlimited.

REPORT DOCUMENTATION PAGE	Form Approved OMB No. 0704-0188

Public reporting burden for this collection of information is estimated to average 1 hour per response, including the time for reviewing instructions, searching existing data sources, gathering and maintaining the data needed, and completing and reviewing the collection information. Send comments regarding this burden estimate or any other aspect of this collection of information, including suggestions for reducing the burden, to Department of Defense, Washington Headquarters Services, Directorate for Information Operations and Reports (0704-0188), 1215 Jefferson Davis Highway, Suite 1204, Arlington, VA 22202-4302. Respondents should be aware that notwithstanding any other provision of law, no person shall be subject to any penalty for failing to comply with a collection of information if it does not display a currently valid OMB control number.
PLEASE DO NOT RETURN YOUR FORM TO THE ABOVE ADDRESS.

1. REPORT DATE *(DD-MM-YYYY)*	2. REPORT TYPE	3. DATES COVERED (From - To)
September 2013	Final	October 2012–March 2013

4. TITLE AND SUBTITLE
High-Maneuverability Airframe: Initial Investigation of Configuration's Aft End for Increased Stability, Range, and Maneuverability

5a. CONTRACT NUMBER

5b. GRANT NUMBER

5c. PROGRAM ELEMENT NUMBER

6. AUTHOR(S)
Sidra I. Silton and Frank Fresconi

5d. PROJECT NUMBER
AH80

5e. TASK NUMBER

5f. WORK UNIT NUMBER

7. PERFORMING ORGANIZATION NAME(S) AND ADDRESS(ES)
US Army Research Laboratory
RDRL-WML-E
Bldg. 459, Mulberry Point Road
Aberdeen Proving Ground, MD 21005-5001

8. PERFORMING ORGANIZATION REPORT NUMBER
ARL-TR-6585

9. SPONSORING/MONITORING AGENCY NAME(S) AND ADDRESS(ES)

10. SPONSOR/MONITOR'S ACRONYM(S)

11. SPONSOR/MONITOR'S REPORT NUMBER(S)

12. DISTRIBUTION/AVAILABILITY STATEMENT
Approved for public release; distribution is unlimited.

13. SUPPLEMENTARY NOTES

14. ABSTRACT
An effort was undertaken to begin development of a high maneuverability airframe for use in the moving target portion of the 2013 U.S. Army Research Laboratory Low-Cost Hyper-Accurate Weapon mission program. To this end, a computational analysis of possible body-fin configurations, with particular emphasis on the aft end of the projectile, was completed to determine the aerodynamic coefficients. For the initial configuration, a complete grid resolution, turbulence model, and computational code version study were completed. The computational aerodynamic coefficients for the body-fin configurations were integrated with previously determined canard aerodynamic coefficients for use in an aerodynamic optimization routine. The aerodynamic optimization routine allowed for approximate determination of necessary fin and canard characteristics to enable a highly maneuverable airframe. The artillery boattail aft end was chosen as the configuration to proceed with for optimization, with the inclusion of canard interaction effects.

15. SUBJECT TERMS
boattail, high maneuverability, airframe optimization, airframe stability, CFD

16. SECURITY CLASSIFICATION OF:			17. LIMITATION OF ABSTRACT	18. NUMBER OF PAGES	19a. NAME OF RESPONSIBLE PERSON
a. REPORT	b. ABSTRACT	c. THIS PAGE			Sidra I. Silton
Unclassified	Unclassified	Unclassified	UU	44	19b. TELEPHONE NUMBER (*Include area code*) 410-306-0792

Standard Form 298 (Rev. 8/98)
Prescribed by ANSI Std. Z39.18

Contents

List of Figures **iv**

List of Tables **v**

Acknowledgments **vi**

1. Introduction **1**

2. Solution Technique **1**

2.1 Computational Aerodynamics 1

2.2 Airframe Optimization Technique 3

3. Model Geometry and Flowfield Conditions **4**

3.1 Model Geometry 4

3.2 Numerical Grids 6

3.3 Flowfield and Boundary Conditions 7

4. Results and Discussion **8**

4.1 Baseline Shoulder-Launched Munition 8

4.1.1 Mesh Wall Spacing and Turbulence Model Study 8

4.1.2 Static Aerodynamic Characterization 13

4.1.3 CFD^{++} Version Comparison 15

4.1.4 Optimization Routine 16

4.2 Geometry Modifications 19

4.2.1 Aerodynamic and Static Stability Comparison 19

4.2.2 Optimization Routine 30

5. Conclusions **33**

6. References **34**

Nomenclature **35**

Distribution List **38**

List of Figures

Figure 1. Three baseline configurations investigated with relevant dimensions: (a) baseline shoulder-launched, (b) artillery aft end, and (c) mortar aft end. 5

Figure 2. Extent of outer mesh boundary with close-up of projectile showing locations of density boxes. 7

Figure 3. Axial force and moment coefficient for C01_V01. 10

Figure 4. Normal force and pitching moment for C01_V01. 11

Figure 5. Velocity contours for (a) cubic *k-ε*, (b) realizable *k-ε*, (c) SST, and (d) *k-ε-R* for C01_V01, Mach 0.65, α = 8°. Scale range from –70 m/s (blue) to 330 m/s (red). 12

Figure 6. Turbulent to laminar viscosity ratio contours for (a) cubic *k-ε*, (b) realizable *k-ε*, (c) SST, and (d) *k-ε-R* for C01_V01, Mach 0.65, α = 8°. Scale range from 0 (blue) to 3800 (red). 13

Figure 7. Aerodynamic coefficients and fits for baseline shoulder-launched munition (C01_V01) at Mach 0.5. 14

Figure 8. Aerodynamic coefficients and fits for baseline shoulder-launched munition (C01_V01) at Mach 0.65. 14

Figure 9. Aerodynamic coefficients and fits for baseline shoulder-launched munition (C01_V01) at Mach 0.8. 15

Figure 10. Optimization analysis for shoulder-launched munition (C01_V01) derivative at Mach 0.65. 17

Figure 11. Aerodynamics from optimization analysis for shoulder-launched munition (C01_V01) variant with $f_F = 1$, $f_C = 0.35$, $x_C = 0.88$ cal. and $\delta = 4°$ at Mach 0.65. 18

Figure 12. Centerline velocity contours, surface pressure coefficients, and streamlines at Mach 0.5, α = 8° for (a) C01_V01, (b) C02_V01, and (c) C03_V01. 25

Figure 13. Comparison of aerodynamic coefficients and derived quantities of each aft-end configuration, version 1, at Mach 0.5. 26

Figure 14. Comparison of aerodynamic coefficients and derived quantities of mortar and artillery configurations with fins on boom at Mach 0.65. 27

Figure 15. Surface pressure coefficients and streamlines at Mach 0.65 and α = 8° for C02_V03 (top) and C03_V02 (bottom). 28

Figure 16. Comparison of aerodynamic coefficients and derived quantities of different versions of artillery configurations with fins on boom at Mach 0.8. 29

Figure 17. Center-line velocity contours and surface pressure coefficients at Mach 0.8, α = 5° for configuration 2 (a) version 1, (b) version 2, (c) version 3, (d) version 4, and (e) version 5. 30

Figure 18. Optimization analysis for artillery aft-end (C02_V01) derivative at Mach 0.65. 31

Figure 19. Aerodynamics from optimization analysis for artillery aft-end (C02_V01) variant with $fF = 1$, $fC = 0.65$, $xC = 0.88$ cal. of X_{cg}, and $\delta = 6°$ at Mach 0.65. 32

List of Tables

Table 1. Configurations investigated. 6

Table 2. Static body-fin aerodynamic coefficient fits for baseline shoulder-launched munition (C01_V01). 15

Table 3. Comparison of aerodynamic coefficients for SST and k-ε-R turbulence model from v11.1.1 and v12.1.1. 16

Table 4. Aerodynamic coefficients per canard blade when f_c = 1.0. 16

Table 5. Static body-alone aerodynamic coefficient fits for artillery aft-end configurations (configuration 2). 20

Table 6. Static total-fin aerodynamic coefficient fits for artillery aft-end configurations (configuration 2). .....**Error! Bookmark not defined.**

Table 7. Static body-alone aerodynamic coefficient fits for mortar aft-end configurations (configuration 3). 22

Table 8. Static total-fin aerodynamic coefficient fits for mortar aft-end configurations (configuration 3). .....**Error! Bookmark not defined.**

Acknowledgments

The author would like to thank the following personnel:

- Ilmars Celmins, U.S. Army Research Laboratory (ARL), for creating the geometries in SolidWorks.
- James DeSpirito for multiple conversations relating to the computational fluid dynamics computations.
- Prasanth Kachgal, Metacomp Technologies, for the discussions and input on turbulence modeling.
- Louisa Fairfax, ARL, Flight Sciences Branch, for performing the technical review.
- The U.S. Department of Defense (DOD) High-Performance Computing Modernization Program (HPCMP) at the U.S. Army Research Laboratory DOD Supercomputing Resource Center (ARL DSRC), Aberdeen Proving Ground, Maryland, for the use of high-performance computing time.

1. Introduction

The 2013 U.S. Army Research Laboratory (ARL) Low-Cost Hyper-Accurate Weapon (LCHAW) mission program is seeking to develop a highly maneuverable projectile that is able to acquire, track, and intercept a moving target. This will require research in a few key areas, including a high-maneuverability airframe and maneuver system as well as vision-based navigation, all at low cost. Prior to engaging in the research on the high-maneuverability airframe and maneuver system, a demonstration platform needed to be selected.

When choosing a demonstration platform for the moving-target mission program it was imperative to find a projectile configuration that would meet stability, range, and maneuverability requirements of the demonstration program while remaining simple enough for quality research to be conducted. Chosen as a starting point was the 83-mm shoulder-launched munition under development at the Armament Research, Development, and Engineering Center (ARDEC) at Picatinny Arsenal, NJ. However, it was unclear if the munition would meet the requirements of the demonstration platform.

The front end of the shoulder-launched munition was simple enough and provided sufficient volume for electronics development as the program progressed. Therefore, it was decided to concentrate initial efforts on modifications to the aft end of the projectile that could possibly allow it to fly in a bank-to-turn or skid-to-turn (i.e., nonrolling) configuration. This report describes the computational fluid dynamics (CFD) and follow-on analyses completed to optimize the body-fin configuration prior to investigating the maneuver system in detail, including the interaction effects between the fins and canards.

2. Solution Technique

2.1 Computational Aerodynamics

The double-precision solver of a commercially available code, CFD^{++} v11.1.1 and v12.1.1 (*1*), was used for the CFD simulations. The basic numerical framework in the code contains unified-grid, unified-physics, and unified-computing features. A brief synopsis of this framework and methodology is given below. The reader is referred to Pulliam and Steger (*2*) and Peroomian et al. (*3*) for further details.

The three-dimensional, Reynolds-averaged Navier-Stokes equations are solved using the following finite volume method (*4*):

$$\frac{\partial}{\partial t}\int_V \boldsymbol{W} dV + \oint [\boldsymbol{F} - \boldsymbol{G}] \cdot dA = \int_V \boldsymbol{H} dV$$

where $\boldsymbol{W}$ is the vector of conservative variables, $\boldsymbol{F}$ and $\boldsymbol{G}$ are the inviscid and viscous flux vectors, respectively, $\boldsymbol{H}$ is the vector of source terms, V is the cell volume, and A is the surface area of the cell face.

The numerical framework of CFD++ is based on the following general elements:

- Unsteady compressible and incompressible Navier-Stokes equations with turbulence modeling (unified-physics).
- Unification of Cartesian, structured-curvilinear, and unstructured grids including hybrids (unified-grid).
- Unification of treatment of various cell shapes including hexahedral, tetrahedral, and triangular prism cells (3-D), quadrilateral and triangular cells (2-D), and linear elements (1-D) (unified-grid).
- Treatment of multiblock patched aligned (nodally connected), patched-nonaligned, and overset grids (unified-grid).
- Total variation diminishing discretization based on a new multidimensional interpolation framework.
- Riemann solvers to provide proper signal propagation physics including versions for preconditioned forms of the governing equations.
- Consistent and accurate discretization of viscous terms using the same multidimensional polynomial framework.
- Point-wise turbulence models that do not require knowledge of distance to walls.
- Versatile boundary condition implementation that includes a rich variety of integrated boundary condition types for the various sets of equations.
- Implementation on massively parallel computers based on the distributed-memory message-passing model using native message-passing libraries or message passing interface, parallel virtual machine, etc. (unified-computing).

The code has brought together several ideas on convergence acceleration to yield a fast steady-state solution methodology for all flow regimes. The approach can be labeled a “preconditioned-implicit-relaxation” scheme. It combines three basic ideas: implicit local time-stepping, relaxation, and preconditioning. Preconditioning the equations ideally equalizes the eigenvalues of the inviscid flux Jacobians and removes the stiffness arising from large discrepancies between the flow and sound velocities at low speeds. However, preconditioning was not used for the geometry investigated here, as it did not improve the convergence characteristics in the subsonic flow regime. Finally, the use of an implicit scheme circumvents the stringent stability limits

suffered by their explicit counterparts, and successive relaxation allows update of cells as information becomes available and thus aids convergence. The suggested ramping of the Courant-Friedrich-Lewy (CFL) number within CFD^{++} also speeds convergence:

- subsonic ($0.3 < M < 0.7$); CFL ramped from 1.0 to 100.0 over 100 iterations.
- transonic ($0.7 < M < 1.4$); CFL ramped from 1.0 to 75.0 over 100 iterations.

Depending on the angle of attack being investigated, the ramping of the CFL number, even at subsonic velocities, had to be limited to 25 or 50. Second-order discretization was used for the flow variables and the turbulent viscosity equation. Turbulence closure is based on topology-parameter-free formulations. Four of the available turbulence models within CFD^{++} were investigated for their ability to accurately predict the aeroballistic coefficients for the geometries and flow conditions investigated for this problem: the two-equation realizable k-ε, cubic k-ε, and shear-stress transport (SST) turbulence models, as well as the Goldberg three-equation k-ε-R turbulence model (*5*). The two-equation realizable k-ε solves the transport equations for the turbulent kinetic energy (k) and its dissipation rate (ε) while accounting for certain known physical properties of the stress tensor by introducing a bound on the magnitude of the predicted tensor components. This has beneficial effects on the stability and improves the predictive accuracy of the model over that of the conventional k-ε model. The nonlinear two-equation cubic k-ε turbulence model also solves the transport equations for k and ε. However, in addition to the enforcement of realizability, the model includes nonlinear terms that account for normal-stress anisotropy, swirl, and curvature effects. The two-equation SST turbulence model solves the transport equation k and the turbulence inverse time scale (ω) in the near-wall regions and blends ω with ε farther away from walls and in the wake region, so that only the dissipation rate is used in the free stream. This method allows the model to be used directly down to the wall without adding any extra damping while remaining less sensitive to the free-stream turbulence properties. The Goldberg three-equation k-ε-R turbulence model solves the transport equations for undamped eddy viscosity (R) in addition to k and ε. This solution methodology accounts for nonequilibrium conditions and avoids free-stream turbulence decay under shear-free flow conditions. Each of these models must be provided initial conditions. A tool exists within CFD^{++} to recommend values for the initialization of the turbulence transport based on user-specified free-stream turbulence intensity (or the turbulent-to-molecular viscosity ratio) and the turbulence length scale. For the current problem the turbulence intensity was set to 2%, and the turbulent-to-molecular viscosity ratio was set to 50 since the length scale was not known.

2.2 Airframe Optimization Technique

The goal of the airframe optimization was to assess the maneuver characteristics of various candidates. Airframe input data (aerodynamics and mass properties) were perturbed to arrive at an optimal configuration. Lift-to-drag ratio, normal force coefficient, and trim angle of attack were often the key metrics for optimization. Canard size, canard location, canard deflection, fin size, fin location, and center-of-gravity location were parameterized from the nominal values.

The approach for the airframe optimization was to first assemble the mass properties and aerodynamics. The body, fin, and canard aerodynamics were often separated to facilitate optimization analysis. Next, the independent parameters of interest were varied. Changing the canard and fin size was accomplished through scaling the axial and normal force coefficients. Canard location, fin location, and center of gravity were varied by properly adjusting the pitching moment coefficient. Once the specific configuration was obtained, the trim angle of attack was found by satisfying a simple moment balance.

$$\sum M = 0 = f_F qSDC_m^F\left(M,\alpha\right) + qSDC_m^B\left(M,\alpha\right) + f_C qSDC_m^C\left(M,\delta+\alpha\right). \tag{2}$$

In this equation, f_C and f_F are the canard and fin scaling factor, q is the dynamic pressure, S is the aerodynamic reference area, D is the reference diameter, C_m is the pitching moment and the superscripts F, B, C and represent the fin, body, and canard, respectively.

The total axial and normal force at this trim angle of attack was determined by the following:

$$C_N\left(M,\alpha_{trim}\right) = f_F C_N^F\left(M,\alpha_{trim}\right) + C_N^B\left(M,\alpha_{trim}\right) + f_C C_N^C\left(M,\delta+\alpha_{trim}\right). \tag{3}$$

$$C_X\left(M,\alpha_{trim}\right) = f_F C_X^F\left(M,\alpha_{trim}\right) + C_N^B\left(M,\alpha_{trim}\right) + f_C C_X^C\left(M,\delta+\alpha_{trim}\right). \tag{4}$$

Finally, the lift-to-drag ratio was calculated from equation 5.

$$L/D = \frac{C_N\left(M,\alpha_{trim}\right)}{tan\left(\alpha_{trim}\right)} - C_X\left(M,\alpha_{trim}\right)tan\left(\alpha_{trim}\right). \tag{5}$$

This optimization approach is relatively general and can be applied to various aerodynamic surfaces with different aerodynamics models. Additionally, this method was implemented to assess the significance of fins or canards in the "+" or "X" configuration.

3. Model Geometry and Flowfield Conditions

3.1 Model Geometry

Seven body-tail configurations were investigated during the course of this study. Each geometry was created in SolidWorks (*6*) and has a body reference diameter of 83 mm. There were three basic configurations and up to five variations of each configuration. The three basic configurations consisted of the baseline shoulder-launched configuration (figure 1a), an artillery aft end (figure 1b), and a mortar aft end (figure 1c). The nose, fin-blade span (distance from the body to the fin tip), and fin axial position from the base of the projectile were kept constant as was the center-of-gravity location (X_{cg}) at 200 mm from the nose for moment calculations. The

nose was always a hemispherical cap. The fin-blade had a maximum chord of 22 mm, a span (from the body) of approximately 81 mm, and a 9.5° leading and trailing edge bevel. The trailing edge was always located 0.38 cal. from the base of the projectile. The baseline shoulder-launch munition had a 2.84-cal.-long cylindrical body, a curved (0.75-cal. radius) boattail 0.76 cal. long, and a 1.08-cal.-long, 0.375-cal.-diameter boom. For the artillery aft end, the body was extended such that the overall length remained the same while creating a 7°, 0.8-cal.-long boattail. The body for the mortar aft end remained the same. The boattail was created by smoothing the area between the body and the base. The result was an approximately 8°, 1.8-cal.-long boattail.

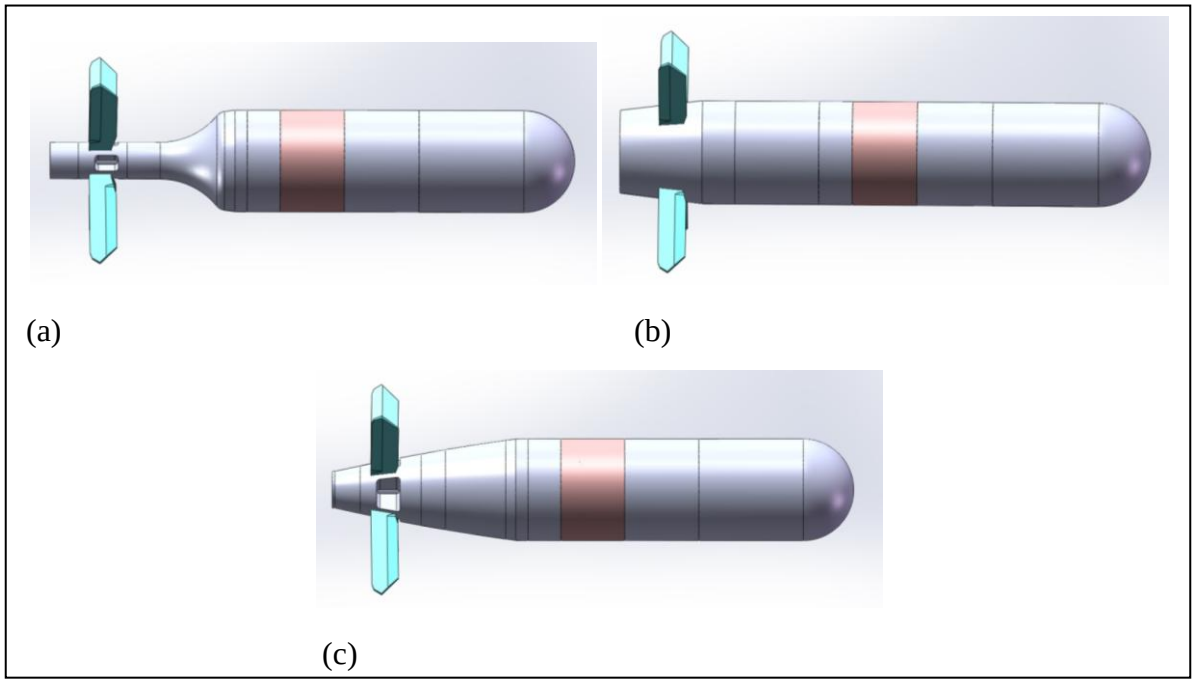

Figure 1. Three baseline configurations investigated with relevant dimensions: (a) baseline shoulder-launched, (b) artillery aft end, and (c) mortar aft end.

Variations including overall length, exclusion of boom, and internal boom were considered. The external boom added to the artillery and mortar aft-end configurations was 1.68 cal. long and the same diameter as the baseline configurations. The internal boom (i.e., cavity) was the same diameter and depth as the external boom. Longer artillery aft-end configurations were created by extending the cylindrical body to obtain the correct overall length. This allowed for a direct comparison (although not necessarily a realistic one) of the configurations. Table 1 shows all of the configurations and variations considered.

Table 1. Configurations investigated.

Config.	Version	Name	Aft End	Boom	Total Fin Span (mm)	Overall Length (mm)	Illustration
1	1	C01_V01	Baseline	External	207.7	428.0147	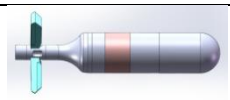
2	1	C02_V01	Artillery	None	239.2	428.0147	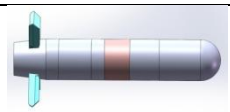
	2	C02_V02		External	239.2	567.7147	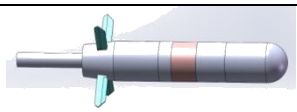
	3	C02_V03		External	207.6	567.7147	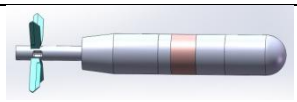
	4	C02_V04		Internal	239.2	428.0147	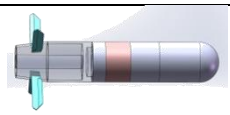
	5	C02_V05		Internal	239.2	567.7147	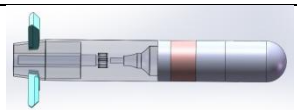
3	1	C03_V01	Mortar	None	207.7	428.0147	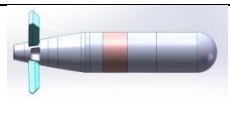
	1	C03_V02		External	207.6	567.7147	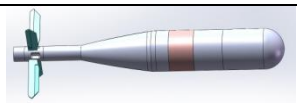

3.2 Numerical Grids

All grids used in the numerical simulation were created with MIME v4.1 by Metacomp Technologies (*7*). MIME is an unstructured mesh generator that allows triangular or quadrilateral dominant cells for the surface mesh. Once an adequate surface mesh is generated, prism layers can be specified and created when the volume mesh is generated. MIME saves a parameter file with the surface names and desired cell sizes that can be used for creating new meshes with similar geometries (as in the present study). One needs only to import the new geometry, open the old parameter file, and assign the geometry as appropriate.

Figure 2 shows the extent of the outer boundary. It extended approximately 35 body lengths from the projectile in all directions. Cylindrical density boxes were placed in the wake of the projectile and fins to ensure proper resolution in this area. Surface mesh and boundary layer growth was restricted to a ratio of 1.2 or less. The growth ratio was relaxed to 2.0 when creating the remainder of the volume mesh. The resulting meshes were contained 14–18 million cells depending on configuration and the first specified prism layer spacing.

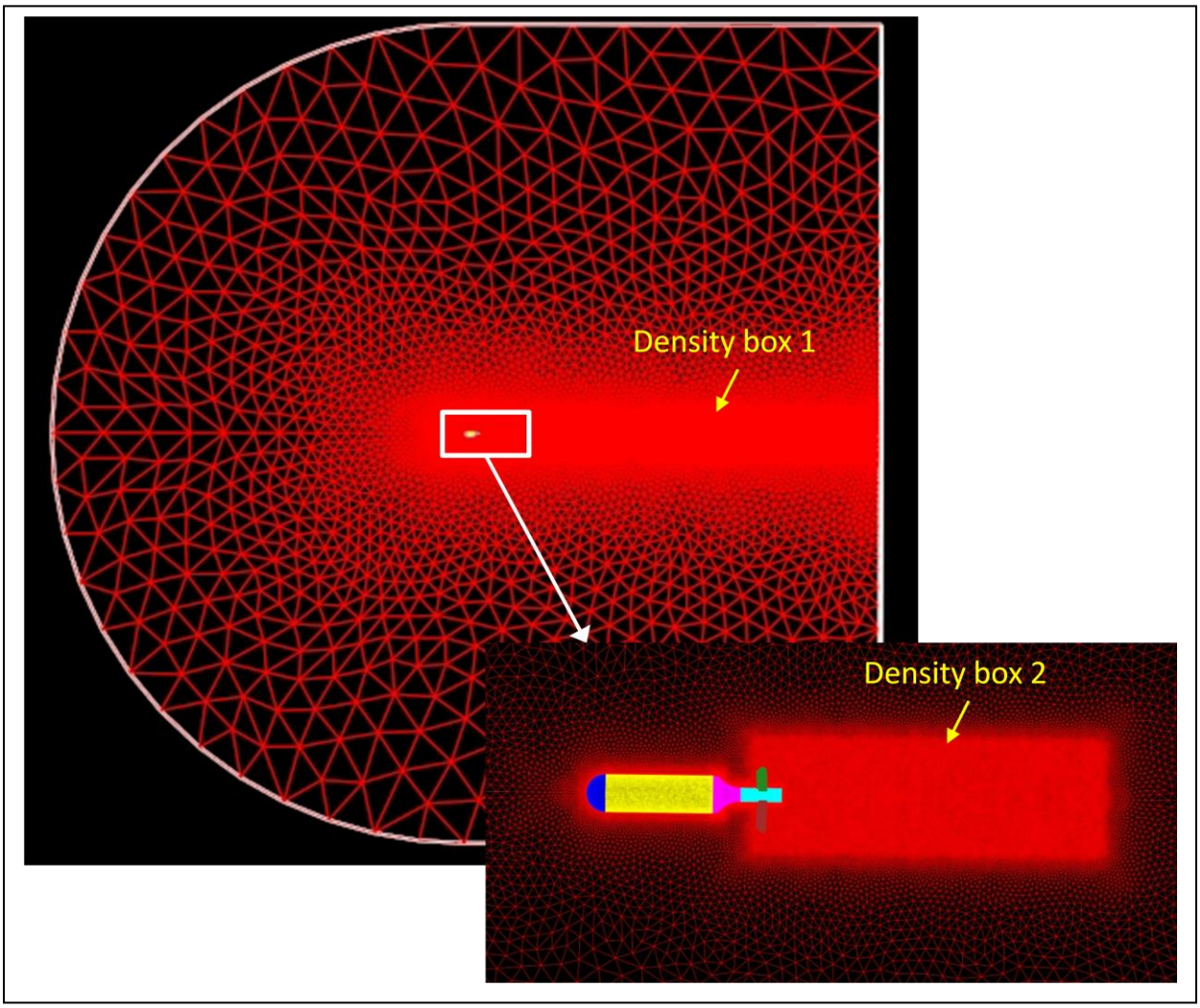

Figure 2. Extent of outer mesh boundary with close-up of projectile showing locations of density boxes.

3.3 Flowfield and Boundary Conditions

All computations were completed using a free-stream temperature and pressure of 288.15 K and 101325 Pa, respectively. During the course of the study, three Mach numbers were investigated: Mach 0.50, 0.65, and 0.80. Seven angles of attack between 0° and 14°, inclusive, were also considered. The domain was initialized using free-stream conditions everywhere. For some cases the area around the projectile was initialized with zero velocity to aid convergence.

The entire far-field boundary was set as “characteristic based” inflow/outflow. This boundary condition takes the specified the free-stream conditions and solves a Riemann problem at the boundary using the supplied data as a virtual state outside the domain. The walls of the projectile were specified as adiabatic, no slip, viscous walls. The wall function integration option was chosen for the projectile surface unless the first prism layer ensured proper integration to the wall. This was only the case for the fins on the final mesh.

4. Results and Discussion

The CFD simulations were completed in two parts. The initial study was carried out on the baseline shoulder-launch configuration as provided by ARDEC (*8*). A grid resolution and turbulence model sensitivity study was conducted as part of the initial study. These initial results were also verified in the most recent version of CFD^{++}, which became available soon after the study began. The aerodynamic (and subsequent static stability) differences between the configurations were determined using the same mesh structure and turbulence model. The aerodynamic results of the body-fin configurations were combined with the relevant canard data to determine the optimum geometry with which to proceed.

4.1 Baseline Shoulder-Launched Munition

The initial computational study was carried out on the baseline shoulder-launched munition (C01_V01), as this was the desired geometry from which to begin. It had recently been fired by ARDEC and was available to ARL through an ongoing U.S. Army Technology Objective. However, there was a limited amount of aerodynamic data available on the configuration from which a flight dynamics model could be built. In order to bound the solution to some extent, it was decided that a turbulence model study as well as a mesh comparison should be completed. Additionally, a new version of the solver became available just after the aerodynamic characterization of the shoulder-launched munition was completed. As such, a limited comparison of the results obtained from the different versions was also completed to ensure that the newer version could be used for the remainder of the study without affecting the results.

4.1.1 Mesh Wall Spacing and Turbulence Model Study

The original mesh specified the first cell spacing for the prism layer (dy) as 0.1 mm everywhere on the projectile body (including the fins). As such, the wall function integration method was specified for all surfaces. While this wall spacing was adequate for most of the geometry at this Mach number (the nondimensional wall spacing was around 30), the nondimensional wall spacing (y^+) around the boom and fins was found to vary from 8 to 15, which are values best avoided as the integration model switches. As such, a second mesh with a dy = 0.25 mm was created. This created a much better wall function mesh at Mach 0.65 with most y^+ values

between values between 20 and 60. However, there was concern that the y^+ values might fall to around 10 again at Mach 0.5. Additionally, after looking closer at the mesh around the fins, it was discovered that the surface mesh on the fins was too fine to support a prism layer built for wall functions (i.e. there was no prism layer on the fins). Therefore, a final mesh was created using a dy = 3.5 μm on the fins. The mesh was transitioned to a dy = 0.3 mm on the boom, dy = 0.25 mm on the body, and 0.2 mm on the nose. This meant that, for the final mesh, solve-to-wall integration was used on the fins while advance wall function was used everywhere else.

The effect of four turbulence closure models on the static aerodynamic coefficients was investigated at Mach 0.65 for 2°, 8°, and 14° angles of attack. They were the cubic k-ε, the realizable k-ε, the k-ε-R, and the SST models. Only the k-ε-R turbulence model was used on the coarser wall function mesh (dy = 0.25 mm).

Comparison of the aerodynamic coefficients for the different grids and turbulence models showed minimal differences. Axial force, C_X, (figure 3, top) shows little variation with either boundary layer spacing or turbulence model proving that the viscous layer is well resolved. There is a bit more variation with axial moment, C_{l_o}, (figure 3, bottom) with turbulence model. This is likely due to how the wake is being resolved and the flow around the beveled fins. However, a 10% variation is not too bad.

Agreement between turbulence models and boundary layer spacing for the normal force coefficient, C_N, (figure 4, top) is quite good and appears to be linear up to α = 14°. The pitching moment, C_m, (figure 4, bottom) shows significant variation with turbulence model than mesh, although the magnitude of the pitching moment was much smaller than was anticipated. The static stability of this round is marginal, at best, and that is before adding the destabilizing effect of canards. The 100% variation in pitching moment makes this configuration marginal at best. However, it is desired to determine which turbulence model is best to move forward with for the remainder of the study. There was also significant variation in the side force and moment. It is not discussed here as it is at least an order of magnitude smaller than the normal force and pitching moment, and was expected to be near zero except perhaps at the larger angles of attack. Its presence may indicate asymmetries in the mesh.

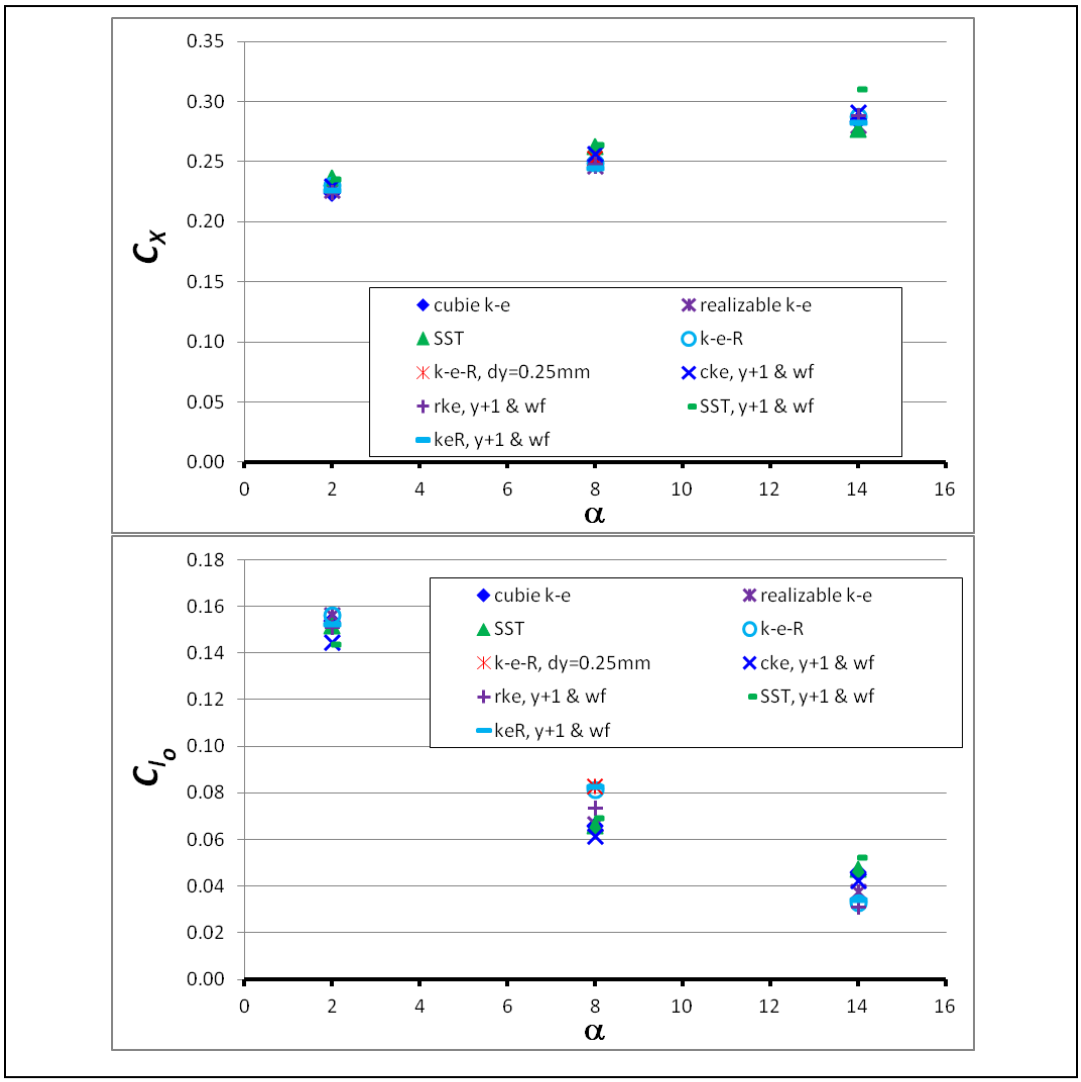

Figure 3. Axial force and moment coefficient for C01_V01.

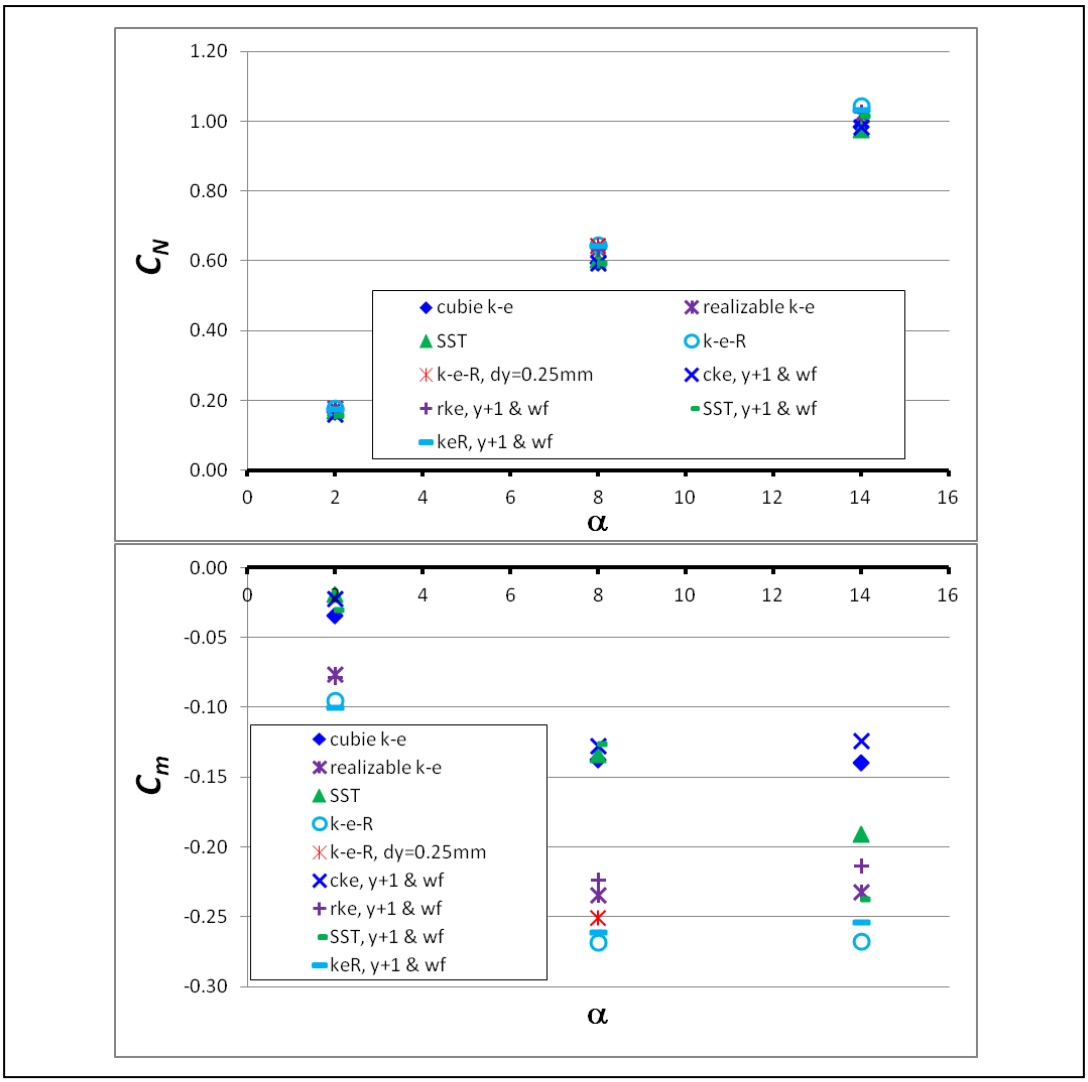

Figure 4. Normal force and pitching moment for C01_V01.

To better understand the reasons for the discrepancies in pitching moment between the turbulence models and determine the best model with which to move forward, the flow field was examined. The velocity and the ratio of turbulent viscosity to laminar viscosity were investigated for each angle of attack. Representative plots at $\alpha = 8°$ are shown for velocity (figure 5) and viscosity ratio (figure 6). Plots at $\alpha = 2°$ and $\alpha = 14°$ were similar. The differences between turbulence models quickly become apparent. The predicted separation bubble, recirculation region, and reattachment points are significantly different, as are the amounts of turbulence present within the recirculation. This is obviously the cause of the variation in pitching moment. It is verified by looking at the contributions to the pitching moment, and the only significant differences occurred on the boom, where flow reattachment occurs. After discussions with the software vendor, it was determined that the k-ε-R turbulence model would likely be the best at predicting this type of flow, as it is similar to a rear-facing step. The two-equation models in CFD++ often over-predict the separated flow region for a rear-facing step. Therefore, lacking experimental validation data for this configuration, the k-ε-R turbulence model will be used for closure for the remainder of the study.

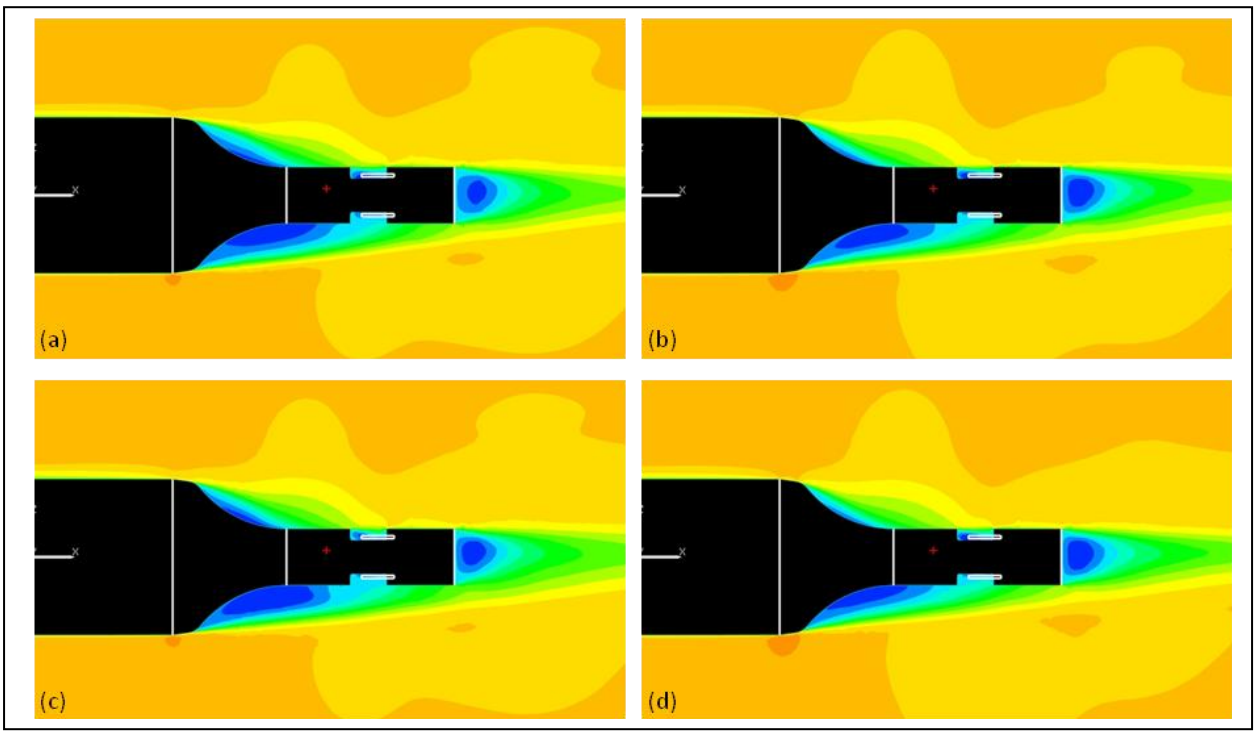

Figure 5. Velocity contours for (a) cubic k-ε, (b) realizable k-ε, (c) SST, and (d) k-ε-R for C01_V01, Mach 0.65, $\alpha = 8°$. Scale range from –70 m/s (blue) to 330 m/s (red).

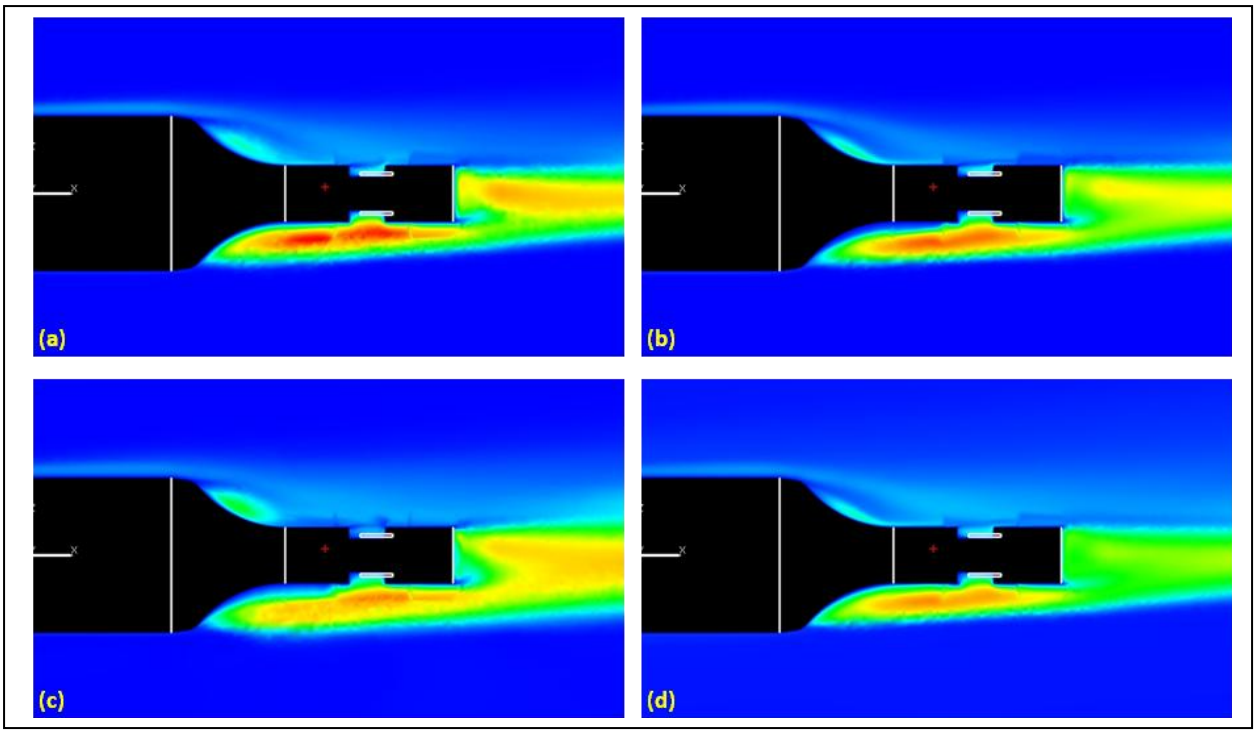

Figure 6. Turbulent to laminar viscosity ratio contours for (a) cubic *k-ε*, (b) realizable *k-ε*, (c) SST, and (d) *k-ε-R* for C01_V01, Mach 0.65, $\alpha = 8°$. Scale range from 0 (blue) to 3800 (red).

4.1.2 Static Aerodynamic Characterization

The static aerodynamic characterization of the baseline shoulder-launched munition was completed using the final mesh (boundary-layer spacing for solve-to-wall integration on fins; wall functions elsewhere) and the *k-ε-R* turbulence closure model. Seven angle-of-attack simulations were completed for each of the three Mach numbers (0.5, 0.65, and 0.8) for a total of 21 simulations. Each simulation was run for enough iterations (typically 3000–5000) to ensure convergence in both residual drop as well as aerodynamic coefficients. The aerodynamic coefficients were then obtained by averaging their values over the last 200 iterations to minimize any oscillations (mostly present at higher angles of attack). The simulations were completed on the IBM iDATAPlex system "pershing" at ARL's Department of Defense Supercomputing Resource Center. The 14.6-million-cell mesh was decomposed using pmetis to run on 96 processors, which resulted in an averaging processing time of approximately 8 s per iteration.

Axial force and roll torque coefficients as well as normal force and pitching moment coefficients were determined at each Mach number and angle of attack. Ballistic fits were completed for the axial force, normal force, and pitching moment coefficients. A third-order polynomial fit was found for the roll-torque coefficients. Figures 7–9 show the ability of the fits to capture the data trends at Mach 0.5, 0.65, and 0.8, respectively. Table 2 lists the values of coefficient derivatives used in the following equations to calculate the total coefficient at each Mach number at angle of attack. These coefficients were used to create the flight dynamics model.

$$C_X = C_{X_0} + C_{X_{\alpha 2}} \delta^2 , \tag{6}$$

$$C_N = C_{N_\alpha} \delta + C_{N_{\alpha 3}} \delta^3 , \tag{7}$$

$$C_m = C_{m_\alpha} \delta + C_{m_{\alpha 3}} \delta^3 , \tag{8}$$

and

$$C_{l_0} = C_{l_0} + C_{l_{01}} \delta + C_{l_{02}} \delta^2 + C_{l_{03}} \delta^3 , \tag{9}$$

where

$$\delta = \sin \alpha . \tag{10}$$

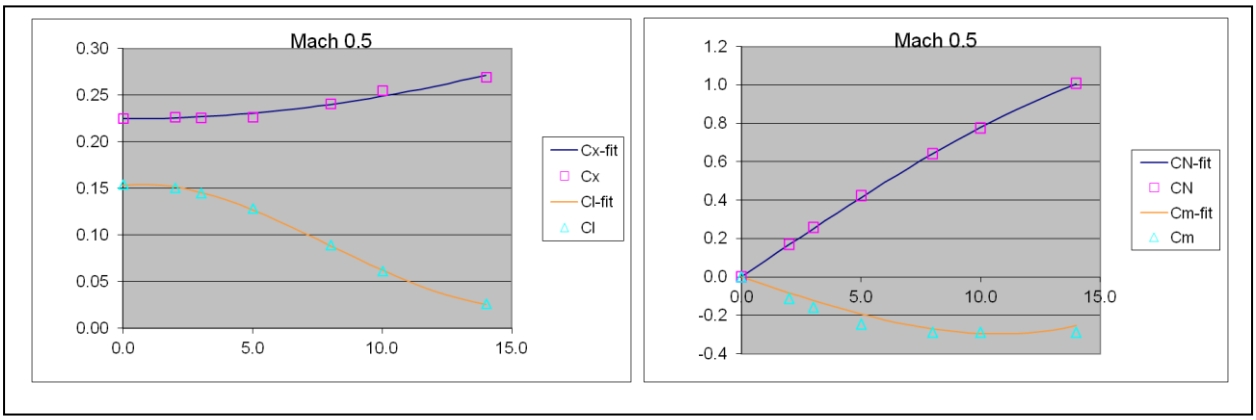

Figure 7. Aerodynamic coefficients and fits for baseline shoulder-launched munition (C01_V01) at Mach 0.5.

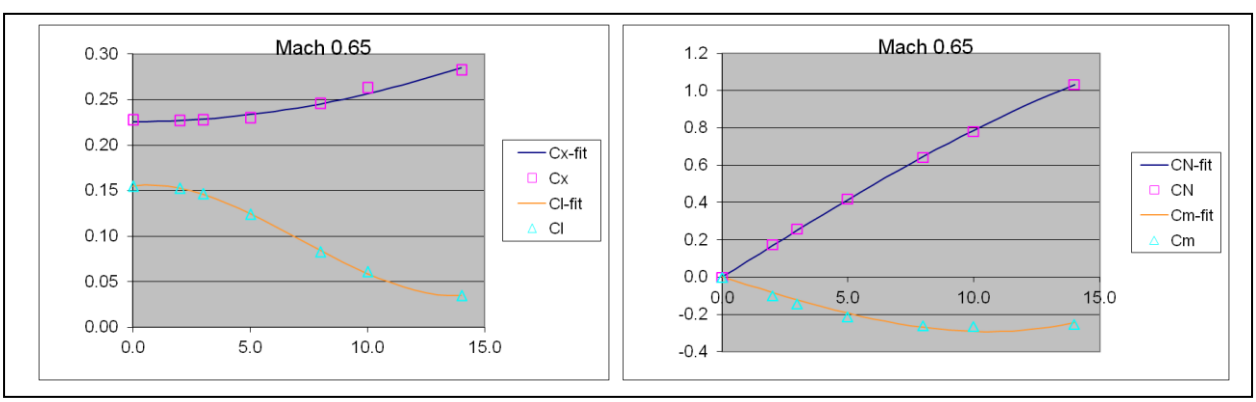

Figure 8. Aerodynamic coefficients and fits for baseline shoulder-launched munition (C01_V01) at Mach 0.65.

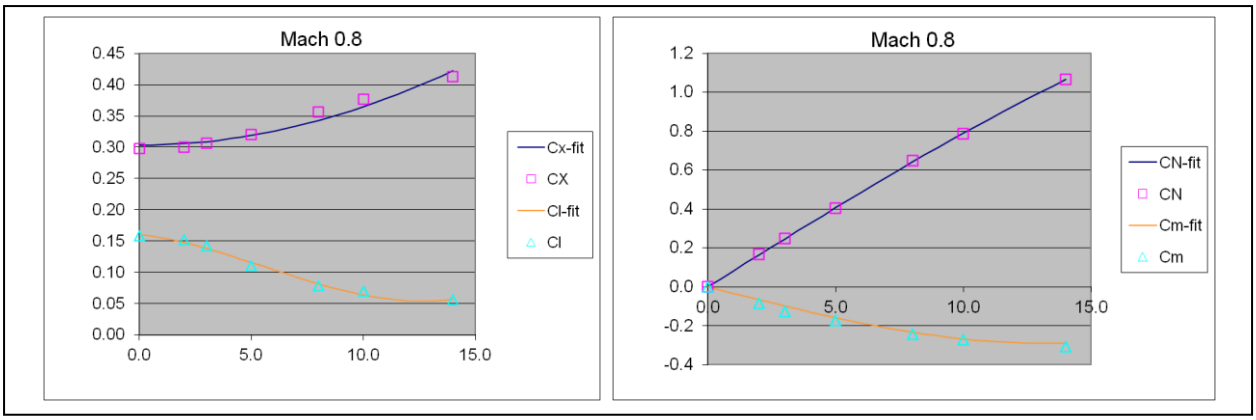

Figure 9. Aerodynamic coefficients and fits for baseline shoulder-launched munition (C01_V01) at Mach 0.8.

Table 2. Static body-fin aerodynamic coefficient fits for baseline shoulder-launched munition (C01_V01).

Mach	C_{X_0}	$C_{X_{\alpha 2}}$	C_{N_α}	$C_{N_{\alpha 3}}$	C_{m_α}	$C_{m_{\alpha 3}}$	C_{l_0}	$C_{l_{01}}$	$C_{l_{02}}$	$C_{l_{03}}$
0.50	0.225	0.803	4.836	–11.703	–2.394	23.017	0.153	0.173	–6.861	16.390
0.65	0.226	1.106	4.840	–9.926	–2.399	23.817	0.155	0.160	–7.655	20.370
0.80	0.303	2.038	4.705	–5.237	–1.911	12.235	0.161	–0.247	–4.434	15.212

The axial force coefficient and, therefore, drag began to grow significantly at Mach 0.8 (figure 9), indicating that the flow was becoming transonic in nature. Although not critical to the flight, this is something that must be kept in mind as round development continues. It may not be desirable to launch the projectile in this flight regime. The aerodynamic coefficients at Mach 0.5 (figure 7) and Mach 0.65 (figure 8) are quite similar as would be expected in compressible, subsonic flow. The most important coefficient to note at all Mach numbers is the small magnitude of the pitching moment. Therefore, although this configuration is statically stable, as indicated by a negative pitching moment, it doesn't have a significant static margin. This suggests that the addition of canards as a maneuver mechanism may not allow for enough (if any) static stability.

4.1.3 CFD^{++} Version Comparison

As the static coefficient study was being completed for C01_V01, CFD^{++} v12.1.1 became available. It was desired to take advantage of the fixes and upgrades in the newer version. Rather than rerun the entire study in the new version, only the final mesh (combined solve-to-wall/wall function) was run for the SST and the *k-ε-R* turbulence models at Mach 0.65 and α = 2°, 8°, and 14°.

The static aerodynamic coefficients were compared for both models and versions (table 3). The SST model was found to predict significant differences in C_m (25%). However, the remainder of the coefficients agreed fairly well (difference of 7% or less). According to Metacomp Technologies, Inc., there was an error in the SST model that was corrected between versions 11.1.1 and 12.1.1 that would account for this difference (9). The differences between almost all

of the coefficients determined from the different versions of the solver were found to be less than 1% for the *k-ε-R* turbulence model. The only exception to this was a 2% difference in C_m at α = 2°. As the *k-ε-R* turbulence model was being used, changing versions is not an issue. As such, all future simulations would be completed in CFD^{++} v12.1.1.

Table 3. Comparison of aerodynamic coefficients for SST and *k-ε-R* turbulence model from v11.1.1 and v12.1.1.

Version	**Turbulence Model**	**α (°)**	C_X	C_ℓ	C_N	C_m
11.1.1	SST	2	0.2358	–0.1436	0.1596	–0.0302
		8	0.2646	–0.0693	0.5954	–0.1260
		14	0.3110	–0.0524	1.0165	–0.2372
	k-ε-R	2	0.2265	–0.1526	0.1744	–0.1002
		8	0.2453	–0.0826	0.6425	–0.2615
		14	0.2825	–0.0342	1.0331	–0.2538
12.1.1	SST	2	0.2364	–0.1482	0.1653	–0.0398
		8	0.2651	–0.0692	0.5951	–0.1254
		14	0.3102	–0.0542	1.0138	–0.2358
	k-ε-R	2	0.2264	–0.1526	0.1740	–0.9868
		8	0.2454	–0.0826	0.6426	–0.2613
		14	0.2823	–0.0344	1.0333	–0.2544

4.1.4 Optimization Routine

This aerodynamic data was combined with solid modeling estimates of mass properties in the airframe optimization technique outlined earlier. Canard aerodynamic data (*10*) was taken from past wind tunnel data on some canard geometries of interest to the current problem (table 4). The desired result of this analysis was optimized maneuverability with the proper canard size, canard location, and canard deflection angle (δ) with the current body and fins.

Table 4. Aerodynamic coefficients per canard blade when f_c = 1.0.

δ (°)	C_{X_0}	CP_X **(cal. from X_{cg})**	CP_R **(cal.)**	C_{N_α}	$C_{N_{\alpha_3}}$	$C_{N_{\alpha_5}}$
0	0.00188	1.134896	0.75	1.1016933	12.08844	–676.216
3	0.00188	1.134896	0.75	0.968886	11.02857	–456.815
6	0.00188	1.134896	0.75	0.915331	11.46496	–354.109
9	0.00188	1.134896	0.75	0.687796	8.092485	–206.117

Optimization results for the baseline shoulder-launched munition geometry are presented in figure 10. The upper left plot shows the optimization metrics of lift to drag, trim angle of attack, and total normal force coefficient as a function of the canard size scaling for a given fin scaling, canard location, and canard deflection angle (specific values shown across top of plot). All metrics are nonlinear with the canard size scaling. The trim angle of attack increases drastically

as the canard size scaling approaches 0.35. The lift-to-drag ratio and normal force coefficient both level out as canard size scaling approaches 0.35 due to canard stall effects. The lift-to-drag ratio peaks at over 2.0, while a body-fin-canard configuration flying without roll motion should be able to reach a lift-to-drag ratio more like 3.0 for a 5-cal. body. The canard size is generally small to maintain proper stability with the shoulder-launched munition geometry. Adding stabilizing fin would be attractive since this enables a larger canard, which provides more controllability, a higher lift-to-drag ration, and greater normal force.

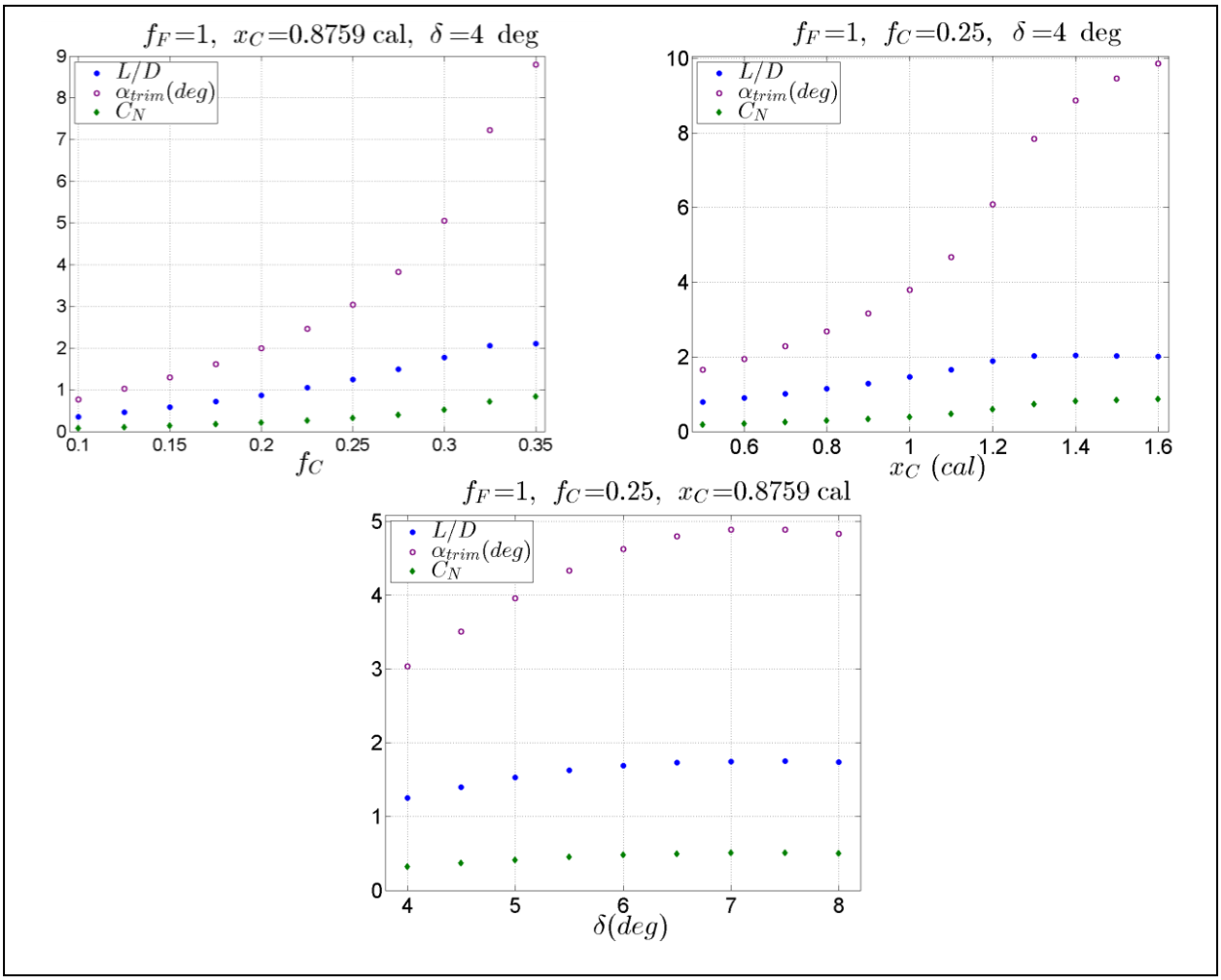

Figure 10. Optimization analysis for shoulder-launched munition (C01_V01) derivative at Mach 0.65.

The effect of canard location is evident in the upper-right plot of figure 10. Again, canard stall effects dictate the peak values of lift-to-drag ratio and normal force. The trim angle of attack does increase slightly past stall. The bottom plot describes the relationship between optimization metrics and canard deflection. A 6°–7° canard deflection appears optimal for this configuration. An example of the baseline shoulder-launched munition configuration aerodynamic estimates that resulted from the optimization analysis ($f_F = 1$, $f_C = 0.35$, $x_C = 0.88$ cal. forward of X_{cg},

and $\delta = 4°$) is provided in figure 11. The contribution to the axial force due to the canards is more than an order of magnitude smaller than the body and fin component. Normal force and pitching moment were calculated for all aerodynamic surfaces in the plane perpendicular to the angle of attack. The four fins and four canards are both in the "X" configuration; therefore, the sum of the components normal to the angle of attack are used to obtain the normal force and pitching moments in the plot. These data illustrate that the body and fins produce the majority of the normal force since the canards are relatively small. Inspection of the pitching moment shows that the trim angle of attack is about 9°. The total pitching moment curve is rather flat with angle of attack so any uncertainty in the aerodynamics drastically changes the trim angle of attack and resulting lift-to-drag ratio and normal force.

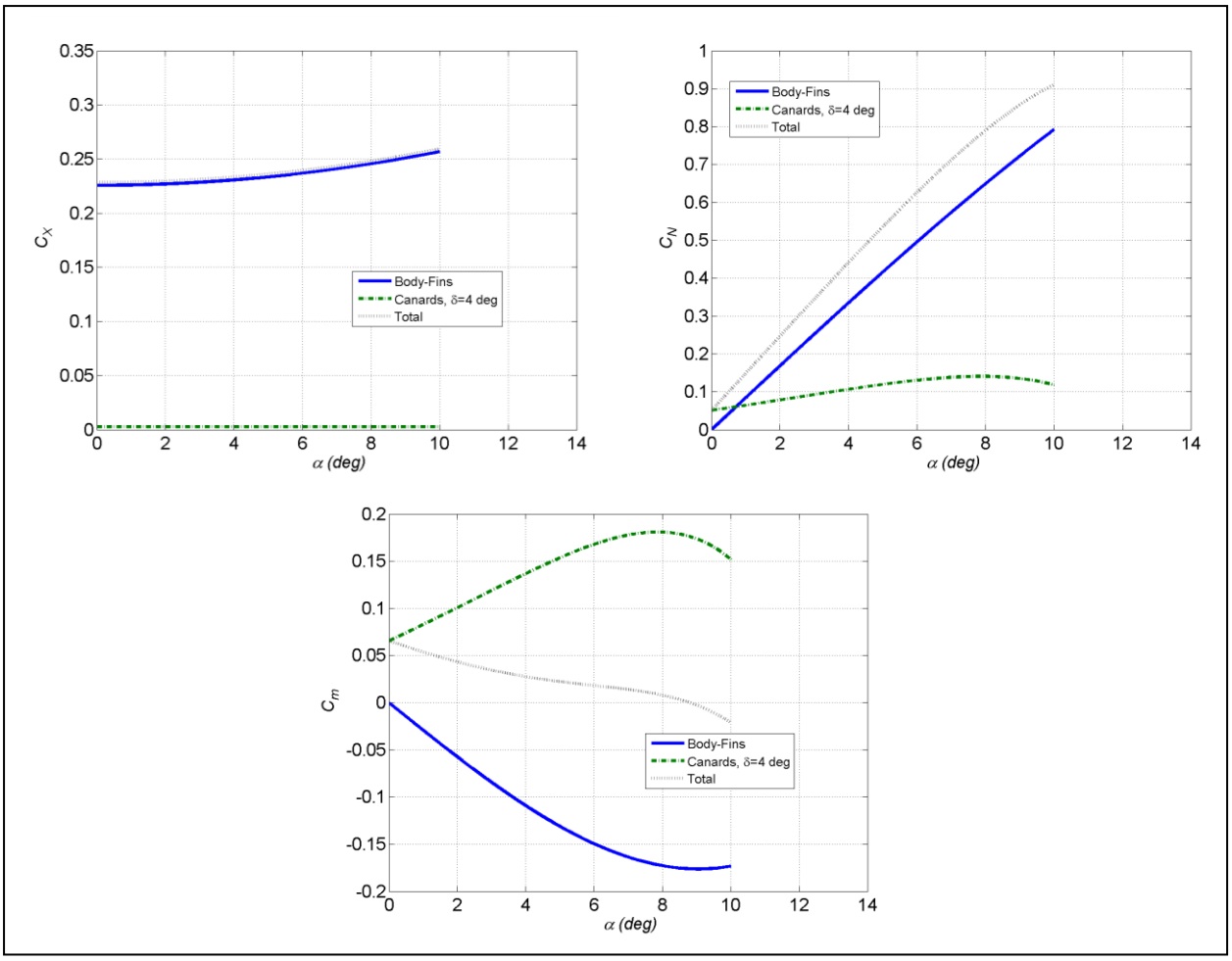

Figure 11. Aerodynamics from optimization analysis for shoulder-launched munition (C01_V01) variant with $f_F = 1$, $f_C = 0.35$, $x_C = 0.88$ cal. and $\delta = 4°$ at Mach 0.65.

In summary, the optimization analysis of the shoulder-launched munition airframe underscores some poor maneuverability characteristics such as small canards necessary for stability, low lift-to-drag ratio, and flat pitching-moment curve. For these reasons, a wider variety of airframe configurations were considered to meet high-maneuverability requirements.

4.2 Geometry Modifications

After determining that the baseline shoulder-launched munition would not meet static stability requirements for a nonrolling, canard-maneuvered airframe, the effect that modifications to the aft end of the projectile would have on performance needed to be investigated. Once again, the aerodynamic investigation would take place only on the body-fin configuration. Specifically, how changes to the aft end only (fin-blade stayed constant) would affect stability, range, and maneuverability needed to be investigated. To this end, two additional aft-end configurations (artillery and mortar) were investigated along with multiple variations of each.

4.2.1 Aerodynamic and Static Stability Comparison

First, the baseline version of each configuration was compared. This meant the overall length of the configurations was constant. The fin span for the artillery aft end (configuration 2) was greater than that of either the shoulder-launched munition (configuration 1) or the mortar aft end (configuration 3) as the fin-blade was kept constant and had to be further off the centerline to accommodate the artillery boattail. The body alone and total fin aerodynamic coefficients for the artillery aft-end configurations are in tables 4 and 5, respectively. Polynomial fits rather than ballistic fits were determined to be best for C_X and C_m and have the form:

$$C_X = C_X + C_{X_{\alpha 1}}\delta + C_{X_{\alpha 2}}\delta^2 + C_{X_{\alpha 3}}\delta^3 + C_{X_{\alpha 4}}\delta^4 \tag{11}$$

and

$$C_m = C_{m_{\alpha 1}}\delta + C_{m_{\alpha 2}}\delta^2 + C_{m_{\alpha 3}}\delta^3 . \tag{12}$$

The body alone and total fine aerodynamic coefficients for the mortar aft-end configurations are in tables 6 and 7. Once again, polynomial fits rather than ballistic fits were used for C_X and C_m.

Table 5. Static body-alone aerodynamic coefficient fits for artillery aft-end configurations (configuration 2).

Config.	**Mach**	C_{X_0}	$C_{X_{\alpha 1}}$	$C_{X_{\alpha 2}}$	$C_{X_{\alpha 3}}$	C_{N_α}	$C_{N_{\alpha 3}}$	$C_{m_{\alpha 1}}$	$C_{m_{\alpha 2}}$	$C_{m_{\alpha 3}}$
C02_V01	0.50	0.158	0	0.799	0	2.547	–2.660	1.117	18.10	–41.93
	0.65	0.156	0	0.847	0	2.680	–2.898	1.276	18.21	–44.21
	0.80	0.225	0	1.701	0	2.374	3.577	2.278	8.068	–23.67
C02_V02	0.50	0.153	–0.0245	0.083	1.228	2.110	2.296	2.164	19.99	–61.61
	0.65	0.150	–0.0224	0.101	1.579	2.217	2.277	2.231	22.14	–71.52
	0.80	0.217	–0.0022	1.521	–0.865	1.916	9.479	3.012	14.51	–58.84
C02_V03	0.50	0.221	–0.0194	1.097	–1.679	1.581	5.800	4.584	–2.166	–7.105
	0.65	0.219	0	1.048	–1.725	1.582	6.330	4.604	–1.224	–9.291
	0.80	0.284	0.004	2.719	–5.577	1.509	7.050	4.257	0.796	–12.279
C02_V04	0.50	0.152	–0.225	3.178	–6.492	2.469	–1.217	1.995	10.75	–25.78
	0.65	0.150	–0.224	3.110	–7.283	2.553	–0.959	2.073	11.53	–29.39
	0.80	0.217	–0.188	4.755	–9.868	2.324	4.502	3.007	1.668	–8.970
C02_V04	0.50	0.168	–0.224	3.313	–7.064	2.480	2.808	0.537	19.28	–53.25
	0.65	0.165	–0.206	3.313	–7.185	2.548	3.409	0.650	20.62	–61.14
	0.80	0.230	–0.169	4.714	–9.855	2.325	8.796	2.368	3.287	–27.09

Table 6. Static total-fin aerodynamic coefficient fits for artillery aft-end configurations (configuration 2).

Config.	**Mach**	C_{X_0}	$C_{X_{\alpha 1}}$	$C_{X_{\alpha 2}}$	$C_{X_{\alpha 3}}$	$C_{X_{\alpha 4}}$	C_{N_α}	$C_{N_{\alpha 3}}$	$C_{m_{\alpha 1}}$	$C_{m_{\alpha 2}}$	$C_{m_{\alpha 3}}$	C_{l_0}	$C_{l_{01}}$	$C_{l_{02}}$	$C_{l_{03}}$
C02_V01	0.50	0.0846	0	0.411	0	0	3.131	–19.09	–9.848	31.20	–41.36	0.233	0.103	–11.15	30.26
	0.65	0.0884	0	0.526	0	0	3.336	–21.06	–9.839	32.81	–48.58	0.245	–0.307	–8.716	26.77
	0.80	0.0961	0	0.678	0	0	3.024	–13.55	–8.924	23.93	–34.40	0.272	–0.967	–4.615	21.39
C02_V02	0.50	0.0844	0	0.400	0	0	3.089	–18.87	–9.681	30.40	–39.68	0.231	0.080	–10.75	28.65
	0.65	0.0882	0	0.508	0	0	3.284	–20.71	–9.706	32.75	–48.30	0.244	–0.313	–8.591	26.08
	0.80	0.0956	0	0.667	0	0	2.958	–13.03	–8.804	24.17	–36.11	0.271	–0.974	–4.458	20.66
C02_V03	0.50	0.00915	0.013	–0.958	6.453	–10.36	3.115	–18.16	–13.64	16.72	25.36	0.154	0.288	–8.350	20.58
	0.65	0.00806	0.024	–1.264	9.419	–17.21	3.245	–19.69	–14.54	24.90	5.006	0.161	0.239	–9.274	25.37
	0.80	0.00750	0.028	–1.465	12.17	–24.64	3.226	–17.88	–14.98	26.24	–0.982	0.168	–0.014	–7.794	24.41
C02_V04	0.50	0.0859	–0.029	0.286	3.079	–8.853	3.110	–18.61	–9.722	30.35	–40.13	0.232	0.077	–11.00	30.11
	0.65	0.0885	–0.025	0.887	–0.411	–3.190	3.310	–20.58	–9.711	31.85	–46.82	0.245	–0.336	–8.555	26.60
	0.80	0.0939	0.017	0.794	1.993	–11.72	3.014	–13.21	–8.69	21.74	–29.33	0.271	–0.977	–4.442	20.91
C02_V05	0.50	0.0856	–0.033	0.371	2.117	–6.413	3.113	–18.77	–16.86	50.19	–60.71	0.230	0.102	–11.21	30.57
	0.65	0.0880	–0.025	0.884	–0.740	–1.976	3.296	–20.59	–16.87	53.22	–73.49	0.243	–0.289	–8.968	27.57
	0.80	0.0936	0.006	0.954	1.177	–10.65	3.02	–13.81	–15.32	37.66	–46.94	0.269	–0.951	–4.498	20.73

Table 7. Static body-alone aerodynamic coefficient fits for mortar aft-end configurations (configuration 3).

Config.	**Mach**	C_{X_0}	$C_{X_{\alpha 1}}$	$C_{X_{\alpha 2}}$	$C_{X_{\alpha 3}}$	C_{N_α}	$C_{N_{\alpha 3}}$	$C_{m_{\alpha 1}}$	$C_{m_{\alpha 2}}$	$C_{m_{\alpha 3}}$
C03_V01	0.50	0.102	0.0370	1.352	–4.718	1.458	3.085	4.201	0.333	–5.608
	0.65	0.0988	0.0421	1.245	–4.268	1.460	3.883	4.296	0.508	–6.390
	0.80	0.171	0.0257	2.002	–4.729	1.355	5.755	4.333	–1.077	–1.827
C03_V02	0.50	0.101	0.0359	1.127	–4.037	1.250	3.754	3.354	1.071	–3.429
	0.65	0.0977	0.0519	0.936	–3.582	1.258	4.302	3.363	1.801	–5.032
	0.80	0.168	0.1008	1.362	–3.534	1.163	5.717	2.891	4.422	–9.871

Table 8. Static total-fin aerodynamic coefficient fits for mortar aft-end configurations (configuration 3).

Config.	**Mach**	C_{X_0}	$C_{X_{\alpha 1}}$	$C_{X_{\alpha 2}}$	$C_{X_{\alpha 3}}$	C_{N_α}	$C_{N_{\alpha 3}}$	$C_{m_{\alpha 1}}$	$C_{m_{\alpha 2}}$	$C_{m_{\alpha 3}}$	C_{l_0}	$C_{l_{01}}$	$C_{l_{02}}$	$C_{l_{03}}$
V01	0.50	0.0796	–0.0235	0.266	0.502	2.775	–14.47	–6.982	9.693	5.282	0.150	0.228	–7.730	19.03
	0.65	0.0819	–0.0320	0.656	–0.598	2.867	–15.12	–7.280	12.73	–3.654	0.156	0.149	–8.299	22.95
	0.80	0.0837	–0.0384	1.302	–2.436	2.791	–11.66	–7.134	10.83	–3.886	0.161	–0.247	–4.439	15.21
V02	0.50	0.0957	–0.0146	0.0610	1.362	3.175	–17.10	–15.16	30.03	–13.94	0.162	0.244	–7.787	18.63
	0.65	0.0990	–0.0104	0.346	0.554	3.378	–19.50	–16.03	37.02	–30.14	0.171	0.175	–8.695	23.52
	0.80	0.102	0.0291	0.726	–0.727	3.415	–17.67	–16.60	35.35	–25.80	0.182	–0.074	–7.765	24.67

Figure 12a shows the C_X for the three configurations at Mach 0.5. As expected, the longer boattail of the mortar configuration has significantly lower axial force. The artillery configuration has significantly more body lift resulting in a greater total normal force for a given angle of attack than the other two configurations (figure 12c). The resulting lift-to-drag ratio is slightly larger for the artillery aft end at $\alpha \leq 6°$ (about 12% at $\alpha = 4°$), but this benefit disappears at larger angles (figure 12e). As such, the maximum range that configuration 2, version 1 (C02_V01), could be expected to achieve should be slightly greater if trim angles remain small. The mortar aft end and the shoulder-launched munition would be expected to achieve approximately the same maximum range based solely on lift-to-drag ratio. The variation in C_{l_0} and C_m (figure 13b and d, respectively) between configurations can be attributed to the tip-to-tip span of the fins and the percentage of the fin-blade that remains in the shadow of the body flow. C_{l_0} is affected only by tip-to-tip span as its value changes only for the artillery aft end where tip-to-tip span is increased. Figure 13 shows the lower pressure that occurs on the fin-blades of the artillery base as it is exposed to the flow, causing the larger roll-torque moments. This lower pressure on the leeward side of the fins on artillery-shaped rounds also causes a more negative pitching moment and, hence, a more stable round. As the flow around the fins on the mortar aft-end shape is similar to that of the shoulder-launched munition, the fin effectiveness is similar as well. The benefit of the mortar shape over the shoulder-launched munition appears to be the elimination of the recirculation region between the boattail and the boom. Unfortunately, the stability of this baseline mortar shape (C03_V01) is no better than that of the original shoulder-launched munition (C01_V01), and at larger angles of attack is actually worse. However, the artillery aft end (C02_V01) shows promise (figure 12d) with a significantly greater static margin. The findings at the higher two Mach numbers were similar.

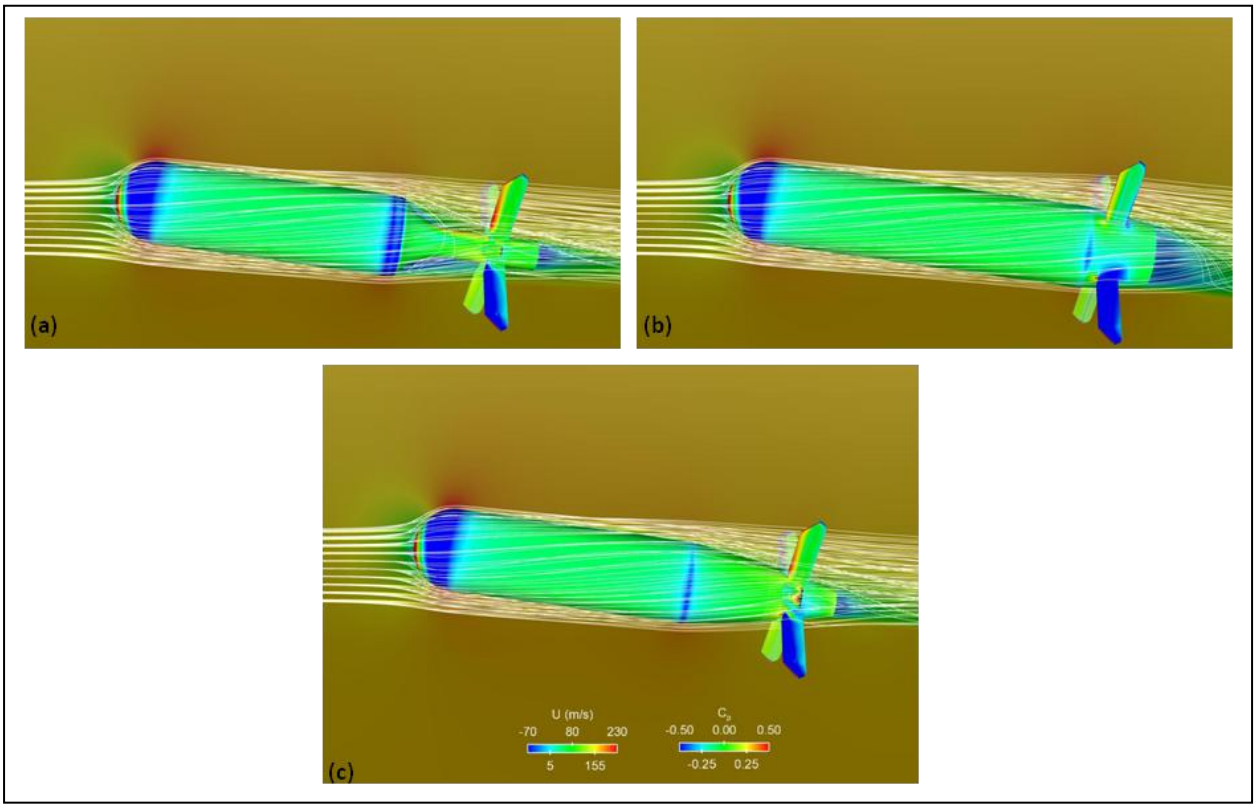

Figure 12. Centerline velocity contours, surface pressure coefficients, and streamlines at Mach 0.5, $\alpha = 8°$ for (a) C01_V01, (b) C02_V01, and (c) C03_V01.

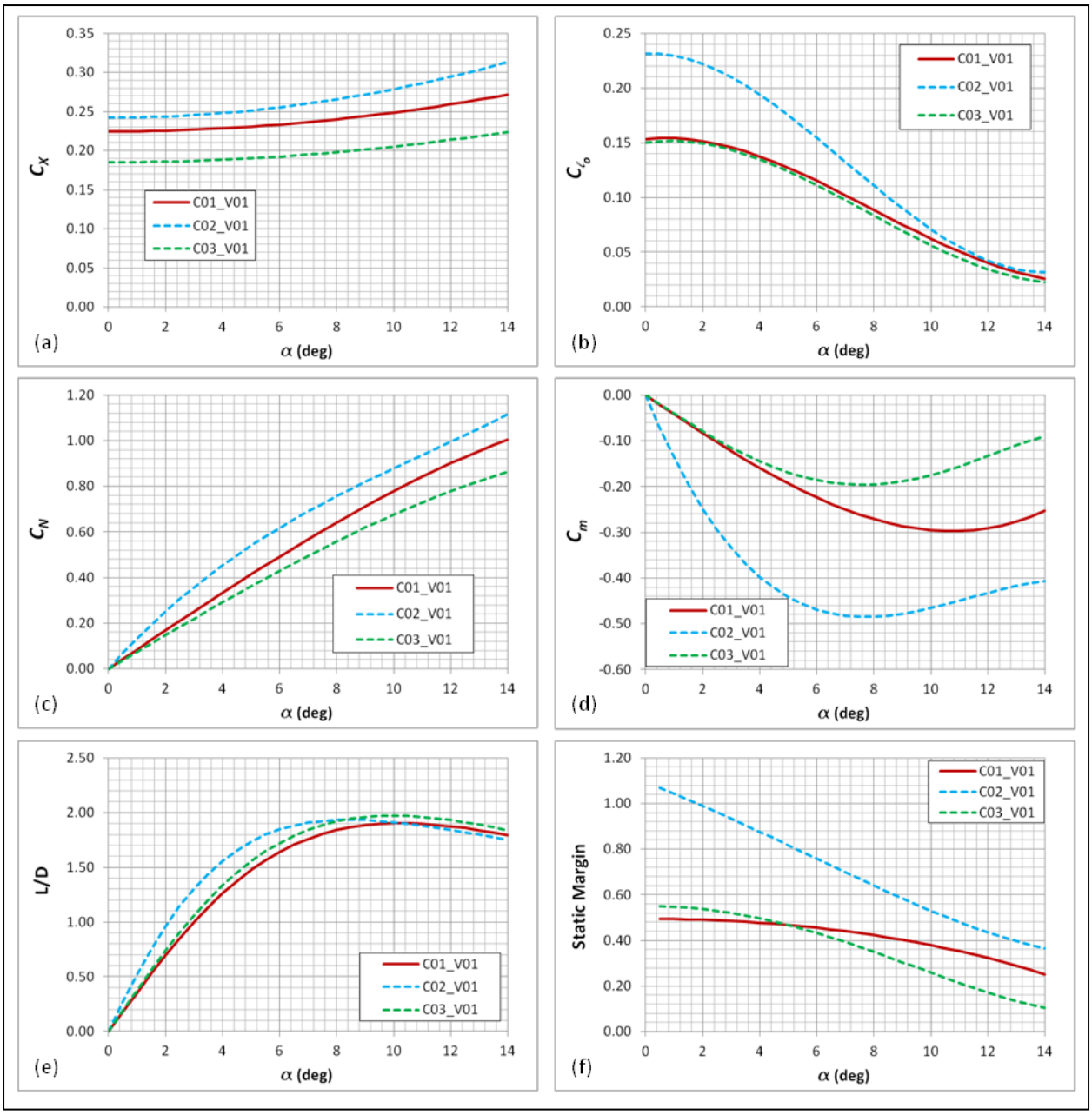

Figure 13. Comparison of aerodynamic coefficients and derived quantities of each aft-end configuration, version 1, at Mach 0.5.

The only significant effect of adding an equal length boom to both the artillery configuration (C02_V03) and mortar configuration (C03_V02), and moving the fins to the end of the boom, was to increase the restoring capability of the pitching moment due to the fins being moved further aft of the projectile center of gravity (figure 14). This, of course, increased the static margin significantly—even over that of having the fins further out in the free stream. The standard mortar configuration (long boattail and fins on boom) appears to have better performance for a longer overall length with the fins on the boom. Figure 15 shows that the long

boattail associated with the mortar aft end does a superior job in turning the flow and directing it toward the fins on the end of the boom, which increases their effectiveness. While the aerodynamics behind the choice of the long boattail when the fins are on the end of the boom may not have been known, the benefits clearly were, as this has been the mortar shape of choice for many years.

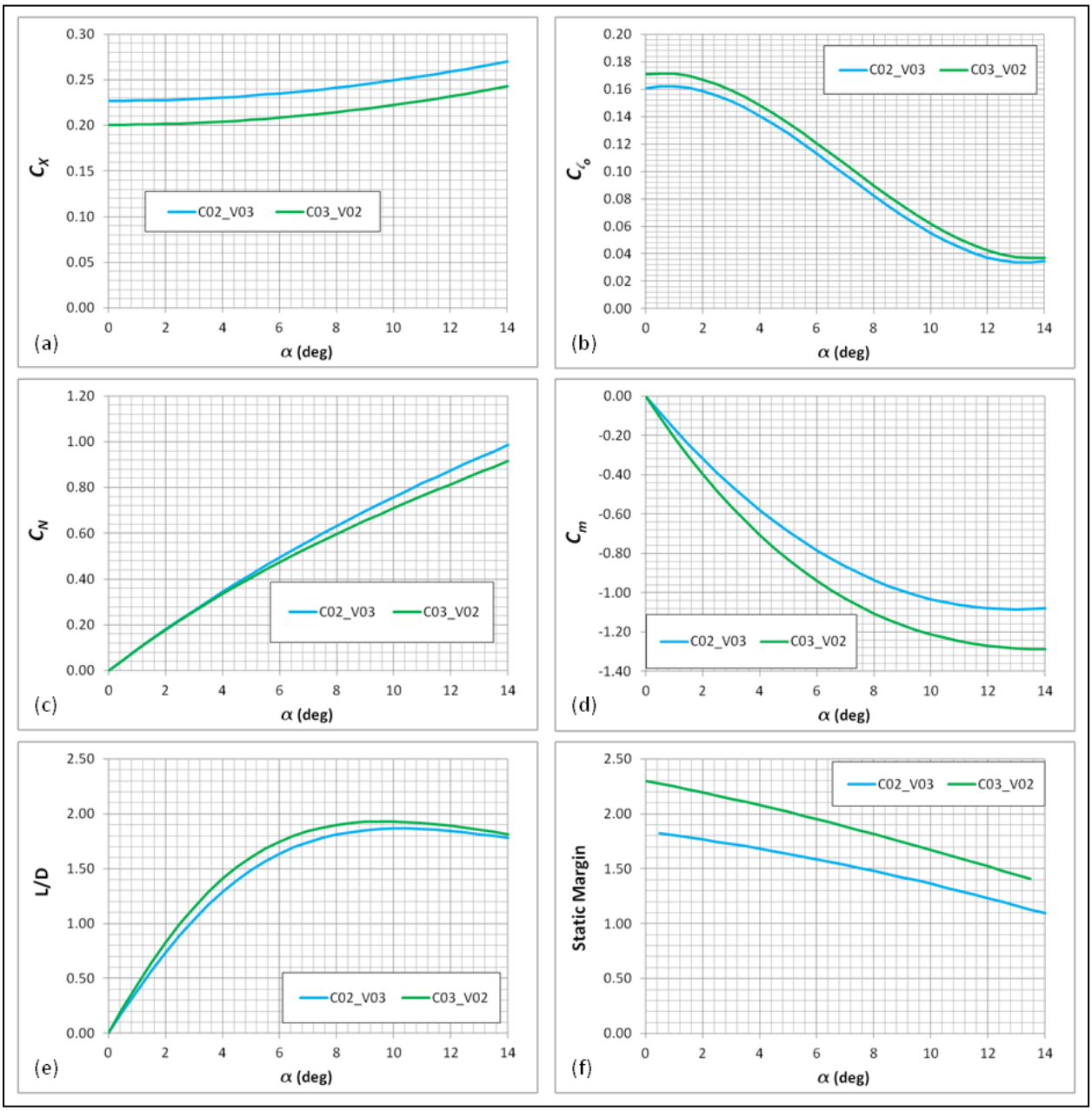

Figure 14. Comparison of aerodynamic coefficients and derived quantities of mortar and artillery configurations with fins on boom at Mach 0.65.

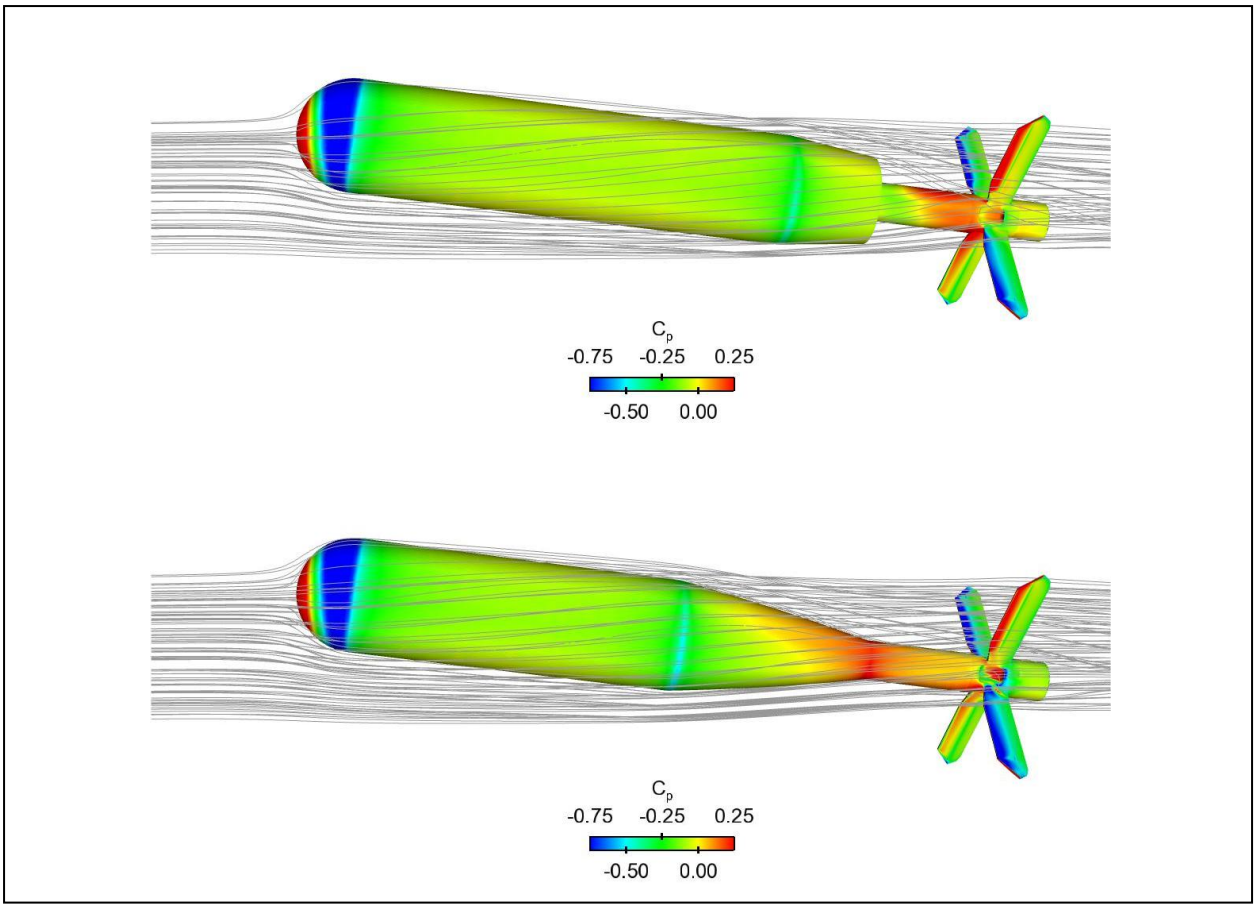

Figure 15. Surface pressure coefficients and streamlines at Mach 0.65 and α = 8° for C02_V03 (top) and C03_V02 (bottom).

Fins on a boom or a longer overall length may or may not be desirable depending on how the projectile is going to be launched or used. Therefore, the effect of an internal or external boom (same projectile length) and longer overall length were investigated (figure 16). It quickly becomes apparent that moving the fins aft either by adding a boom or elongating the projectile makes the projectile more stable (more negative C_m) as the fins are farther from the projectile center of gravity. This is to be expected. Just increasing the overall length of the projectile (fins remain on the boattail) has a minimal effect on any of the other aerodynamic coefficients. However, when the fins are moved to the end of the boom the tip-to-tip fin span is decreased, which has the effect of decreasing C_{l_0}, C_N, and C_X (slightly). Whether this is a positive or negative effect depends on what one is trying to accomplish, but it is definitely noticeable. Figure 17c shows this decrease is likely due to the fins being almost completely in the shadow of the body. This decreases their effectiveness, as indicated by the significantly different pressure contours on both the windward and leeward sides of the fins. The three remaining versions attempt to quantify the effect of the boom itself, with the fins remaining on the boattail. The flow is different only if an external boom is present (figure 17); the wake region is effectively elongated. Because the flow effects are confined to the wake, the presence of the boom had

minimal effect, if any, on the aerodynamic performance of the projectile. Based on the present study, the artillery aft end with the fins on the boattail appears to have better overall performance. If boom-mounted fins are required, the mortar configuration is likely the best configuration.

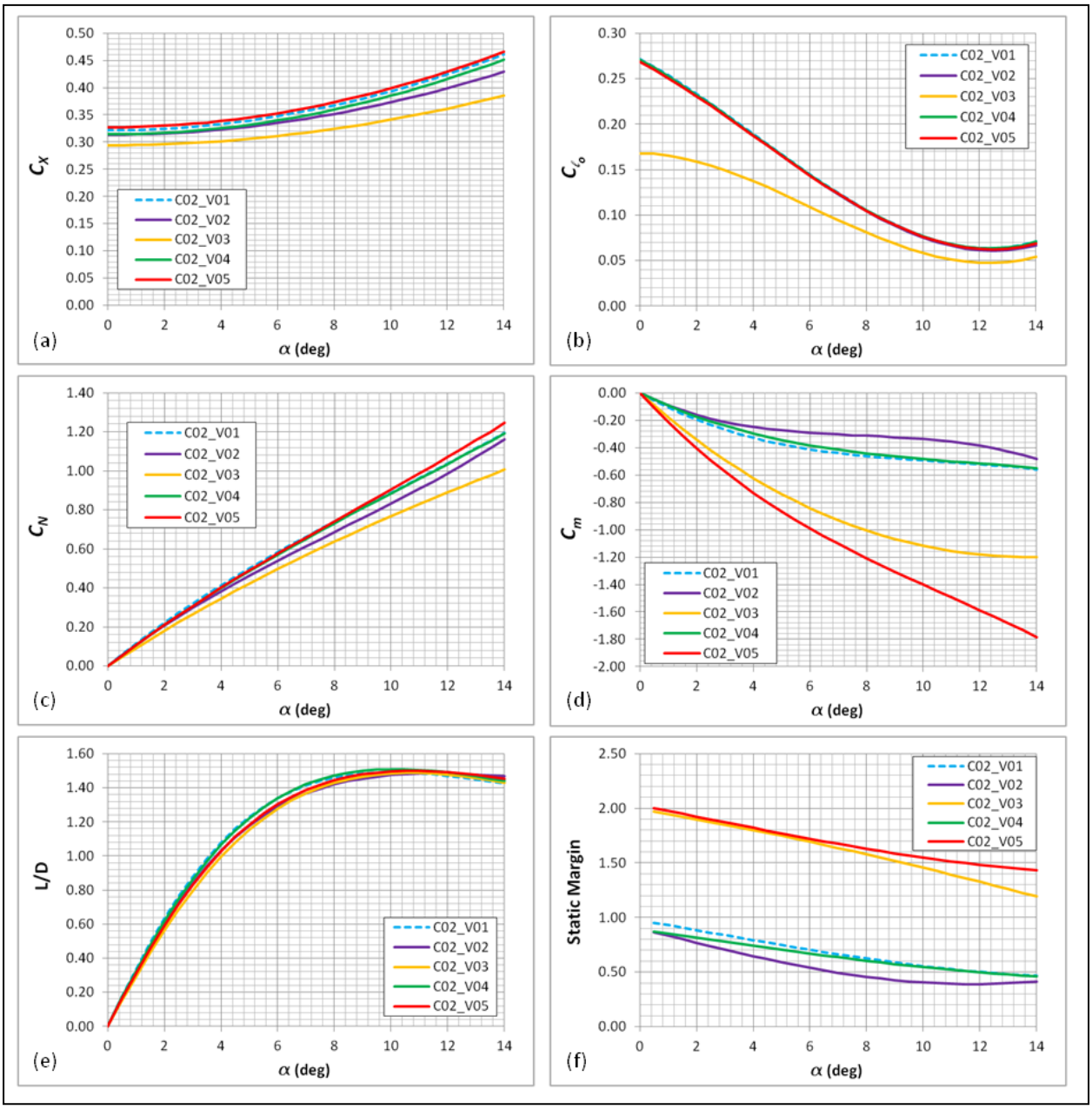

Figure 16. Comparison of aerodynamic coefficients and derived quantities of different versions of artillery configurations with fins on boom at Mach 0.8.

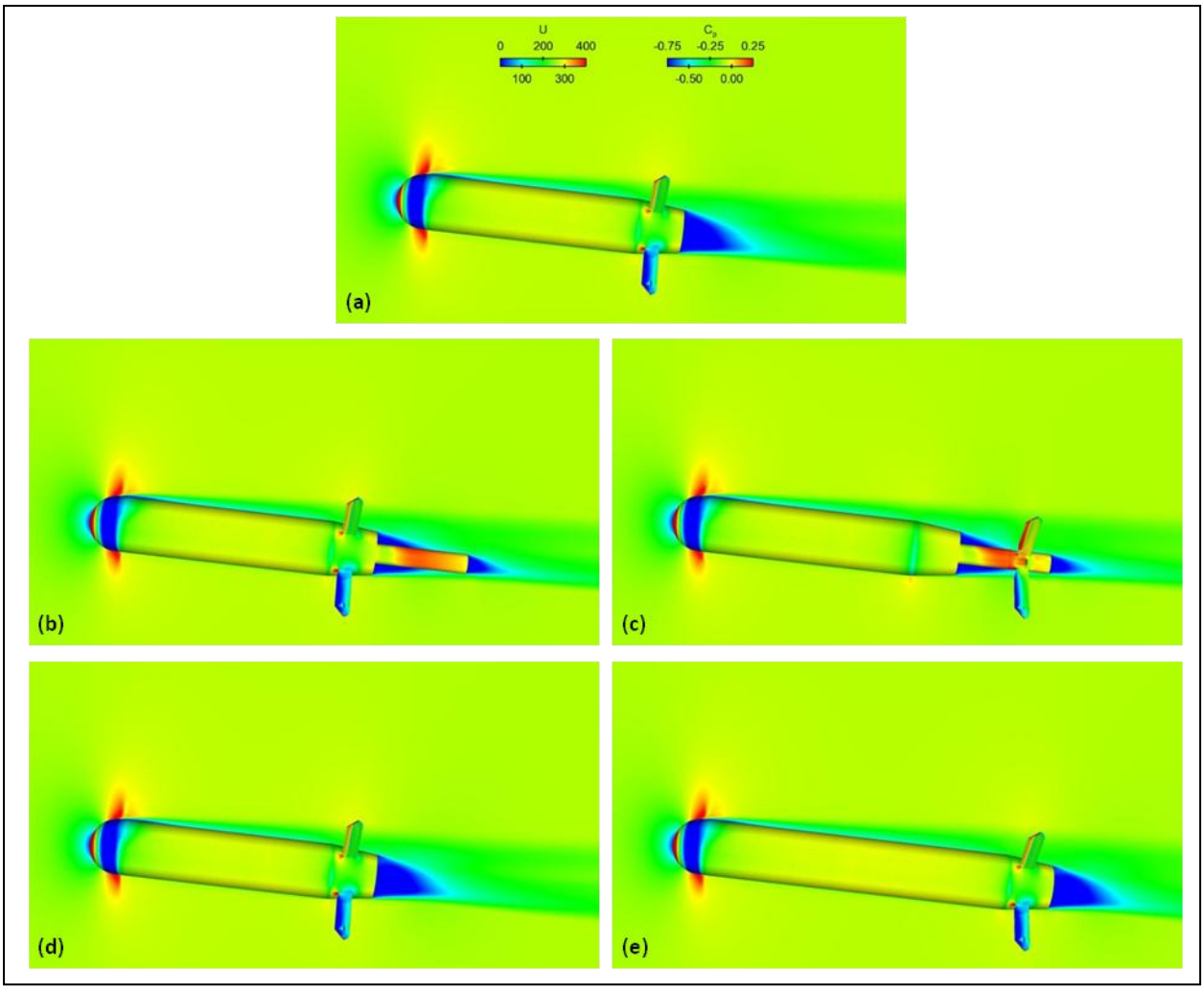

Figure 17. Center-line velocity contours and surface pressure coefficients at Mach 0.8, $\alpha = 5°$ for configuration 2 (a) version 1, (b) version 2, (c) version 3, (d) version 4, and (e) version 5.

4.2.2 Optimization Routine

The optimization routine was again employed on the computational aerodynamics data for the alternate configurations. Results are shown for one version of the artillery aft end (C02_V01) as it was the most promising candidate. The same canard wind tunnel data used previously were superposed with the CFD data for the body and fin to analyze the total airframe.

The relationships among the optimization metrics and canard size, canard location, and canard deflection are given in figure 18. The nonlinear trends introduced in the description of the data in figure 10 apply to the present data. Canard stall effects interact with the body and fin aerodynamics to yield optimal canard size, canard location, and canard deflection. Larger canards may be used for this configuration due to greater fin stability, which provides a lift to drag ratio well over 2.0 and normal force coefficient of about 1.0.

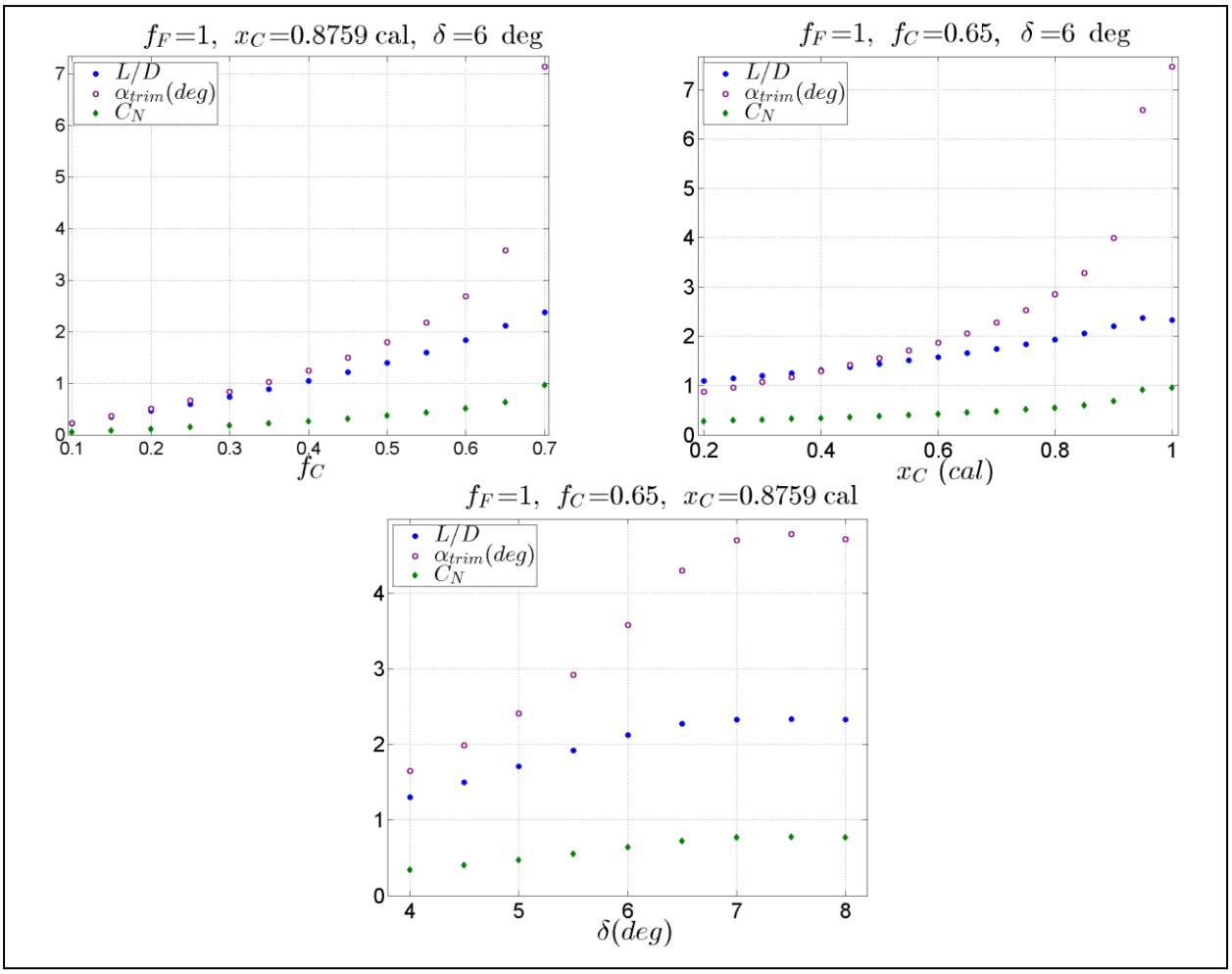

Figure 18. Optimization analysis for artillery aft-end (C02_V01) derivative at Mach 0.65.

Configuration aerodynamics resulting from the optimization analysis are presented in figure 19. Similar to the data for the shoulder-launched munition, the axial force of the canards is much smaller than that of the body and fins. Comparing figure 11 with figure 19 illustrates that the canard normal force is a larger contributor to the overall normal force since the greater fin stability facilitates larger canards. The total pitching moment is still flat, which raises some concern about the suitability of the design margin with respect to uncertainty.

Analysis of the optimal airframe suggests an artillery aft end with proper selection of fins and canards might provide the best maneuverability with a 5-cal. body. The optimal parameters, which produced a very flat pitching-moment curve indicating a sensitive design, were were $f_F = 2$ and $f_C = 0.45$ with the canards located located 0.88 cal. forward of X_{cg} and and $\delta = 6°$. Physical constraints of the airframe space claims will likely limit the size and placement of the canards.

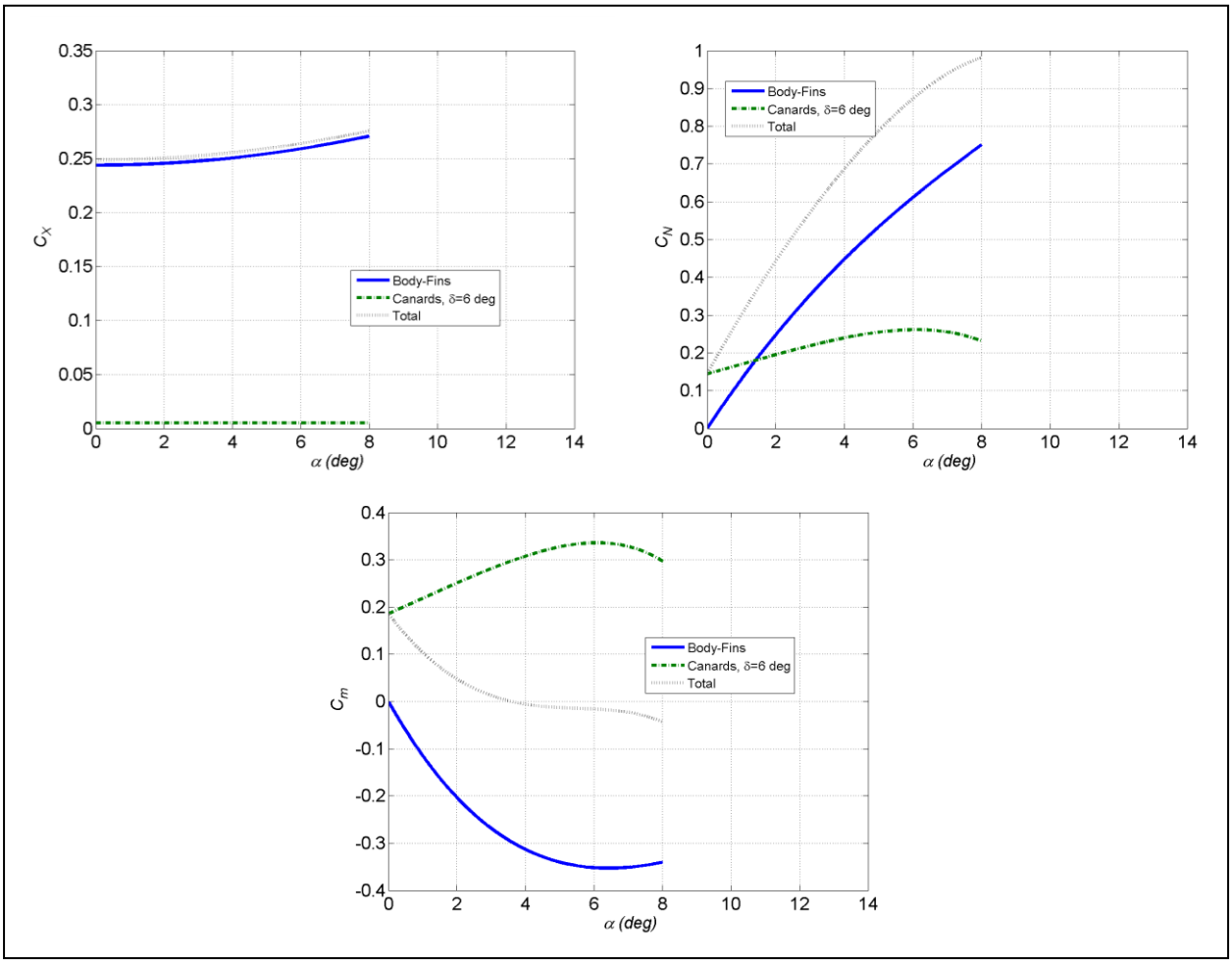

Figure 19. Aerodynamics from optimization analysis for artillery aft-end (C02_V01) variant with $f_F = 1$, $f_C = 0.65$, $x_C = 0.88$ cal. of X_{cg}, and $\delta = 6°$ at Mach 0.65.

5. Conclusions

CFD was used to determine the aerodynamic performance of three aft-end configurations, as well as multiple variants of each, while retaining the same fin-blade and fore-body geometry, thereby isolating the effects of the aft end. For a constant overall length, the lift-to-drag ratio was found to be nearly constant between the configurations. The short boattail of an artillery aft end was found to provide the best static margin. When the overall length was increased, due to extending the body or adding a boom with the fins on the end of the boom, the long shallow boattail of a mortar aft end was found to be the most beneficial.

The aerodynamic optimization routine used a component buildup methodology and drew on the new, computationally determined aerodynamic coefficients and previously obtained canard aerodynamic coefficients to determine if the body-fin configurations would provide enough maneuverability while remaining statically stable. Without accounting for any interaction effects between the fins and canards, the artillery aft-end configuration was determined to be the most promising; the canards on the original shoulder-launched munition would have had to have been too small. The results of the aerodynamic optimization routine, along physical constraints, will be used as a starting point for the detailed investigation of the maneuver system to develop the complete high-maneuverability airframe.

6. References

1. Metacomp Technologies, Inc., *CFD^{++} User Manual*; Agoura Hills, CA, 2011.
2. Peroomian, O.; Chakravarthy, S.; Goldberg, U.; *A 'Grid-Transparent' Methodology for CFD*; AIAA Paper 97-07245; 1997.
3. Peroomian, O.; Chakravarthy, S.; Palaniswamy, S.; Goldberg, U.; *Convergence Acceleration for Unified-Grid Formulation Using Preconditioned Implicit Relaxation*; American Institute of Aeronautics and Astronomics Paper 98-0116; Reston, VA, 1998.
4. Pulliam, T. H.; Steger, J. L.; On Implicit Finite-Difference Simulations of Three-Dimensional Flow, *AIAA Journal* **1982**, *18* (2), 159–167.
5. Goldberg, U. C.; Peroomian, O.; Chakravarthy, S.; A Wall-Distance-Free k-ε Model With Enhanced Near-Wall Treatment. *ASME Journal of Fluids Engineering* **1998**, *120*, 457–462.
6. Dassault Systems SolidWorks Corporation. *SolidWorks 2012*; Waltham, MA, 2012.
7. Metacomp Technologies, Inc. *MIME User Manual*; Agoura Hills, CA, 2010.
8. Okken, D.; Vazquez, E.; U.S. Army United States Army Armament Research, Development and Engineering Center, Picatinny Arsenal, NJ. Private communication, 8 January 2013.
9. Kachgal, Prasanth. Metacomp Technologies. Private communication, 03 January 2013.
10. DeSpirito, J.; U.S. Army Research Laboratory, Aberdeen Proving Ground, MD. Private communication, March 2012.

Nomenclature

k	turbulent kinetic energy
ε	dissipation rate
R	undamped eddy viscosity
ω	turbulence inverse time scale
f_c	canard-scaling factor
f_F	fin-scaling factor
q	dynamic pressure, , $\frac{1}{2}\rho V^2$
ρ	density
V	velocity magnitude
D	reference diameter
S	aerodynamic reference area, $\frac{\pi D^2}{4}$
C_m	pitching moment coefficient
C_N	normal force coefficient
C_X	axial force coefficient
C_{l_o}	axial moment (roll torque) coefficient
M	Mach number
α	angle of attack
α_{trim}	trim angle of attack
δ	canard deflection angle (or $\sin\alpha$ where defined in total coefficient equations)
X_{cg}	center of gravity location
x_c	canard center-of-pressure location
L/D	lift-to-drag ratio
C_p	pressure coefficient
dy	first cell spacing off wall
y^+	nondimensional wall spacing

Superscripts

F	fin
B	body
C	canard

NO. OF COPIES	ORGANIZATION
1 (PDF)	DEFENSE TECHNICAL INFORMATION CTR DTIC OCA
1 (PDF)	DIRECTOR US ARMY RESEARCH LAB IMAL HRA
1 (PDF)	DIRECTOR US ARMY RESEARCH LAB RDRL CIO LL
1 (PDF)	GOVT PRINTG OFC A MALHOTRA
2 (PDF)	RDRL WML E S SILTON F FRESCONI